CERN - EUROPEAN ORGANIZATION FOR NUCLEAR RESEARCH

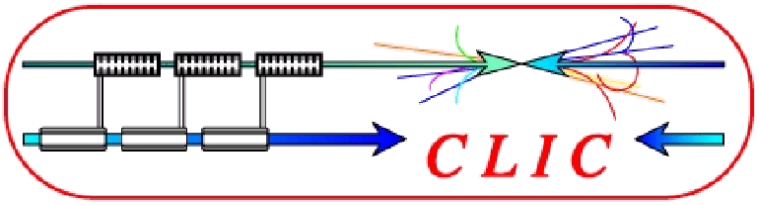

CLIC Note 704

EUROTeV-Report-2007-001

CERN-OPEN-2007-005
06/02/2007

Conceptual design of a post-collision transport line for CLIC at 3 TeV

A. Ferrari,
Uppsala University, Sweden

Strong beam-beam effects at the interaction point of a high-energy linear collider such as CLIC lead to an emittance growth for the outgoing beams, as well as to the production of beamstrahlung photons and e^+e^- coherent pairs. We present a conceptual design of the post-collision line for the nominal CLIC machine at 3 TeV, which separates the various components of the outgoing beam thanks to a vertical magnetic chicane, before transporting them to their respective dump.

Geneva, Switzerland
February 6, 2007

1 Introduction

The Compact Linear Collider (CLIC) aims at multi-TeV e^+e^- collisions [1] using the two-beam acceleration technology. In order to keep the length (and the cost) of the machine at a reasonable level, the accelerating gradient and the RF frequency are 150 MV/m and 30 GHz, respectively. The bunch spacing is thus a few cm only, which is far too short to allow head-on collisions. Actually, the optimal crossing angle for CLIC is 20 mrad [2]. In order to force the colliding bunches to be perfectly aligned (and thereby to recover the desired luminosity), crab cavities must be used, which deflect the head and the tail of each bunch in opposite horizontal directions upstream of the interaction point. In a high-energy e^+e^- linear collider such as CLIC, the incoming beams must be focused to extremely small spot sizes in order to achieve high charge densities and, in turn, to reach the desired luminosity. As a result, the colliding beams experience very strong electromagnetic fields at the interaction point. The subsequent bending of their trajectories leads to the emission of beamstrahlung photons, which can then turn into e^+e^- coherent pairs. A careful design of the post-collision extraction lines must be performed in order to transport the charged particles and the beamstrahlung photons from the interaction point to the dump, with as small losses as possible.

The extraction line considered for the 20 mrad configuration of the International Linear Collider (ILC) consists of a DFDF quadruplet, just downstream of the interaction point, followed by two vertical magnetic chicanes for energy and polarization measurements, and a long field-free region allowing the beam to grow naturally before it reaches the dump [3]. Such a design is not adapted to CLIC, because of the larger amount of low-energy particles found in both the disrupted beam and the coherent pairs, which would lead to much larger power losses than at ILC [4]. Instead, we propose a design based on the separation of the disrupted beam, the beamstrahlung photons and the coherent pairs, just downstream of the interaction point, followed by a transport to the dump through dedicated extraction lines.

In Section 2, we review the main parameters of the incoming beams at CLIC, as well as the outgoing beam distributions at the interaction point. In Section 3, we discuss the extraction and separation of the different components of the outgoing beam. Then, we study the transport of the disrupted beam, of the beamstrahlung photons and of the coheremt pairs to the dump in Section 4. The power losses in the post-collision line are then studied as a function of beam-beam offsets at the interaction point. Finally, a summary and outlooks are given in Section 6.

2 Incoming and outgoing beam distributions at the interaction point

The incoming beam parameters of the nominal CLIC machine (i.e. for a centre-of-mass energy of 3 TeV) are given in Table 1.

Parameter	Symbol	Value	Unit
Center-of-mass energy	E	3	TeV
Particles per bunch	N_b	2.56	10^9
Bunches per RF pulse	n	220	
Bunch spacing	Δt_b	0.267	ns
Repetition frequency	f	150	Hz
Primary beam power	P_b	20.4	MW
Horizontal normalized emittance	$(\beta\gamma)\epsilon_x$	660	nm.rad
Vertical normalized emittance	$(\beta\gamma)\epsilon_y$	10	nm.rad
Horizontal rms beam size	σ_x	60	nm
Vertical rms beam size	σ_y	0.7	nm
Rms bunch length	σ_z	30.8	μm
Peak luminosity	L	6.5	10^{34} cm^{-2} s^{-1}

Table 1: Incoming beam parameters of the nominal CLIC machine [5].

The outgoing beam distributions at the interaction point were derived from GUINEA-PIG simulations [6], with 10^5 macro-particles. The transverse distributions of the CLIC disrupted beams are shown in Figure 1, in the case of ideal e^+e^- collisions. The double-peak shape of the x' distribution is characteristic for collisions with flat beams. The strong beam-beam interactions lead to an increase of the angular divergence, and thereby to a significant emittance growth at the interaction point (in both transverse directions). As for the energy spectrum of the CLIC disrupted beams, it is shown in Figure 2. The long low-energy tails result from the emission of beamstrahlung photons during the bunch crossing. Simulations performed with GUINEA-PIG indicate that, in average, 1.1 beamstrahlung photons are emitted per incoming electron or positron. As for the beamstrahlung parameter δ_B (the average energy loss of each incoming beam through the emission of photons), it is 16% at CLIC.

In the presence of a strong electromagnetic field, beamstrahlung photons can turn into e^+e^- coherent pairs. The probability associated to their production depends essentially on the parameter Υ defined as [7]:

$$\Upsilon = \frac{5}{6}\,\frac{\gamma r_e^2 N_b}{\alpha\sigma_z\sigma_y(1+\sigma_x/\sigma_y)}, \tag{1}$$

where $\alpha = 1/137$ and $r_e = 2.82 \times 10^{-15}$ m are respectively the fine-structure constant and the classical electron radius.

At CLIC, $\Upsilon \simeq 3.6$ and the expected number of e^+e^- coherent pairs, derived from GUINEA-PIG simulations, is 4.6×10^7 per bunch crossing. The transverse distributions of such pairs are shown in Figure 3. The electrons and positrons of the coherent pairs carry typically about 10% of the primary beam energy, as it is shown in Figure 4.

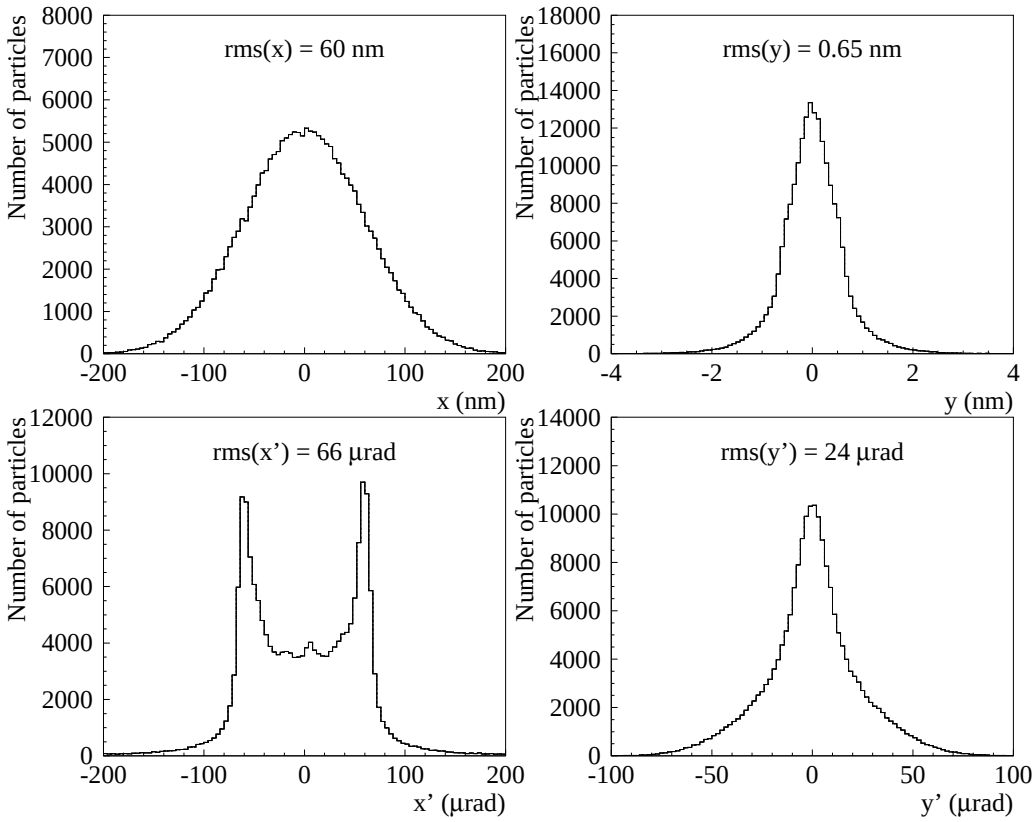

Figure 1: Transverse distributions of the disrupted beam at the interaction point of the nominal CLIC machine.

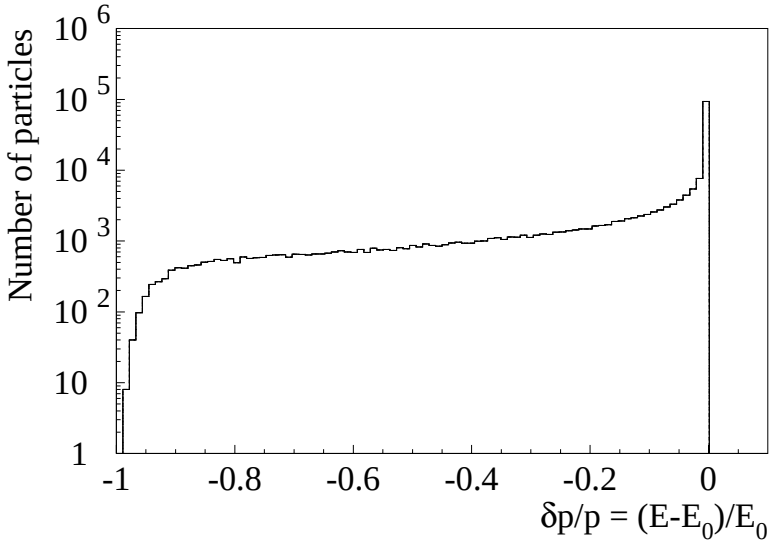

Figure 2: Energy spectrum of the disrupted beam at the interaction point of the nominal CLIC machine.

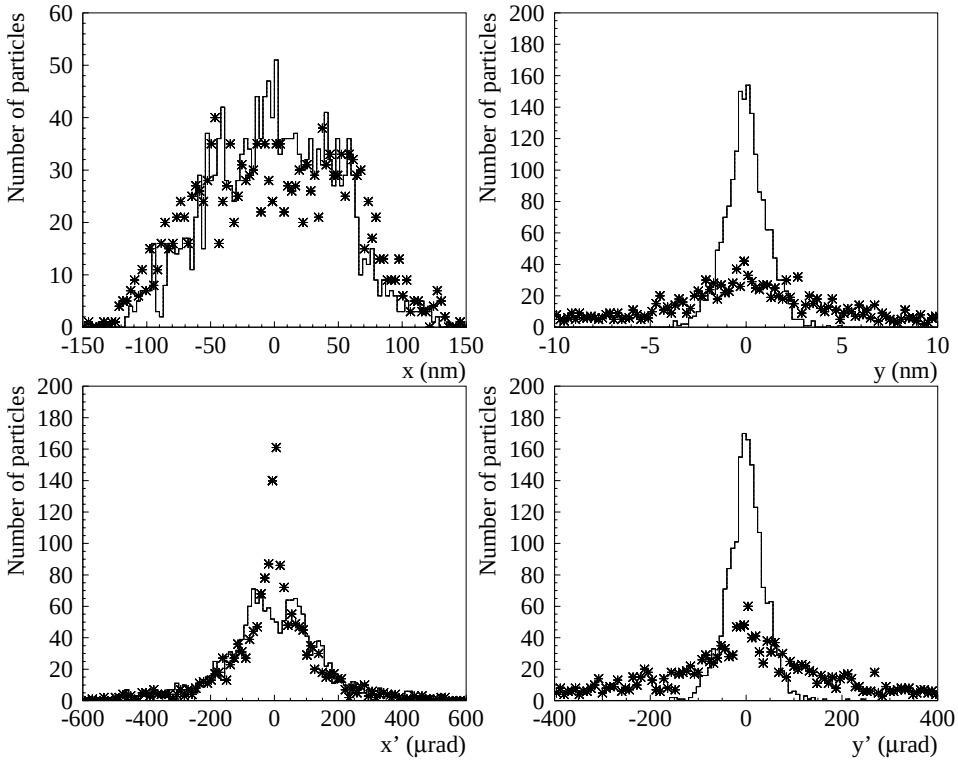

Figure 3: Transverse distributions of the coherent pairs at the interaction point of the nominal CLIC machine. Full lines correspond to particles that have the same charge as the disrupted beam, while stars correspond to the opposite charge.

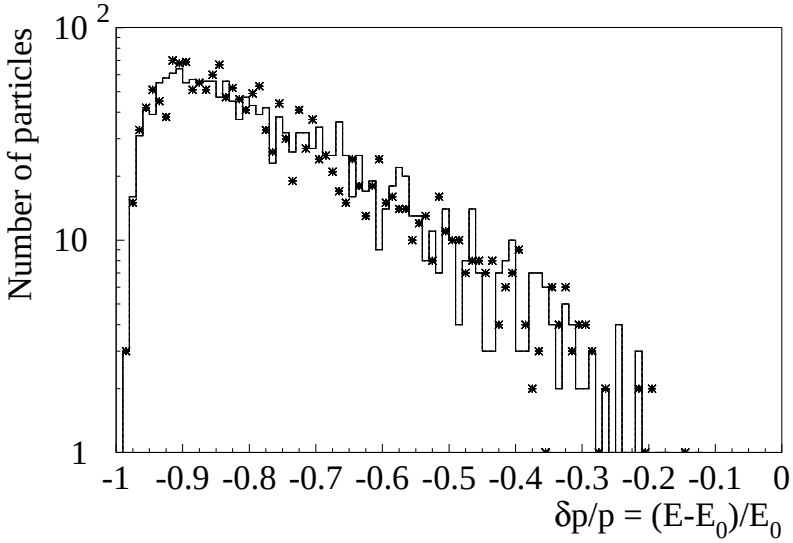

Figure 4: Energy spectrum of the coherent pairs at the interaction point of the nominal CLIC machine. Full lines correspond to particles that have the same charge as the disrupted beam, while stars correspond to the opposite charge.

3 Extraction and separation of the various components of the CLIC outgoing beam

At CLIC, the incoming beams must be focused to extremely small spot sizes in order to achieve the design peak luminosity of 6.5×10^{34} cm^{-2} s^{-1}. The nominal horizontal and vertical rms sizes of the colliding beams are respectively 60 and 0.7 nm. For this purpose, very low transverse emittances must be achieved, but one must also force the betatron functions to reach very small values at the interaction point: β_x(IP) and β_y(IP) are respectively 7 and 0.09 mm. At a distance s downstream of the interaction point, the betatron functions of the undisrupted beam are given by:

$$\beta(s) = \beta(IP) \times \left[1 + \left(\frac{s}{\beta(IP)}\right)^2\right]. \quad (2)$$

Because of the very low values of β_x(IP) and β_y(IP), the betatron functions downstream of the interaction point become rapidly very large.

In the nominal configuration of the ILC with a centre-of-mass energy of 1 TeV, the horizontal and vertical betatron functions at the interaction point are 3 cm and 0.3 mm, respectively [8]. The first elements of the 20 mrad extraction are quadrupoles. They are placed close to the interaction point and are therefore very compact. In addition, their settings aim at creating a secondary focus point for the undisrupted beam, in the middle of the second vertical chicane [3]. If a similar solution was envisaged for CLIC, either the quadrupoles would have to be even closer to the interaction point, or their strength would have to be somewhat larger than in the ILC case, since smaller betatron functions at the interaction point mean a faster increase downstream of the corresponding waist. In any case, since the beam disruption (and thereby the extension of the low-energy tails and the amount of e^+e^- coherent pairs) are greater at CLIC than at ILC, the presence of quadrupoles just downstream of the interaction point would lead to unacceptable losses. Indeed, low-energy particles tend to be over-focused in the quadrupoles and eventually leave the vacuum pipe. Then, by interacting with the surrounding matter, they may damage the magnetic elements and produce back-scattered particles, which can become a significant background for the detector. One way to reduce these losses is to lower the strength of the quadrupoles. However, the design optics at the nominal energy is destroyed and, as a result, the secondary focus point disappears. A detailed estimation of the power losses of a nominal CLIC beam in the ILC 20 mrad extraction line was performed in [4]. It clearly suggests that an alternative type of extraction line should be investigated. The design that we propose is based on the separation by a magnetic chicane of the disrupted beam, the beamstrahlung photons and the e^+e^- coherent pairs, just downstream of the interaction point. Obviously, since the chicane magnets bend the electrons in one direction and the positrons in the other direction, they can not be horizontal, due to the presence of the incoming beam line. We must therefore consider vertical bending magnets and they must be as compact as possible.

3.1 Conceptual design of post-collision extraction magnets

For the extraction of the different components of the outgoing beam, we consider so-called window frame magnets. A schematic layout of their cross section is shown in Figure 5, together with the geometrical parameters that are relevant for their design.

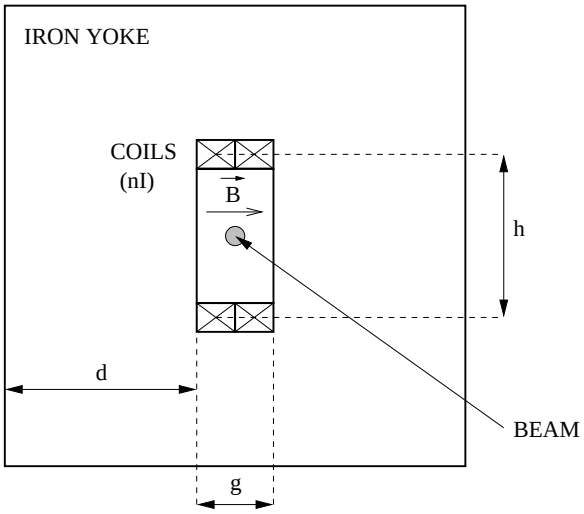

Figure 5: Cross section of a window frame magnet, with the relevant parameters to be considered for its design.

Here, we assume that the field strength grows linearly from 0 to B along the coils. The air gap in the middle of the iron yoke has to be large enough in order to accept all components of the outgoing beam. There, the magnetic flux Φ is given by:

$$\Phi = h\,\ell\,B, \tag{3}$$

where ℓ stands for the longitudinal length of the magnet.

Let us now write Ampere's law inside the magnet. If nI is the number of Ampere-turns circulating in the coils, then one has:

$$nI = \oint \mathbf{H}\cdot d\mathbf{s} = \frac{B}{\mu_0}\,g + \int_{iron} \frac{B_{iron}}{\mu_r\mu_0}\,ds. \tag{4}$$

If there is no saturation in the iron yoke, the second term can be neglected, so the magnetic field B depends only on the gap g and on the current in the coils. One must however make sure that the iron yoke is large enough in order to allow the magnetic flux to fully return through it. If the maximal field strength in the iron is B_{max}, then one must impose:

$$d \geq \frac{\Phi/2}{\ell B_{max}} \Longrightarrow d \geq h \times \frac{B}{2B_{max}}. \tag{5}$$

We now focus on the extraction of the three components of the outgoing beam. Let us first assume that only one extraction dipole magnet is used, as in Figure 6.

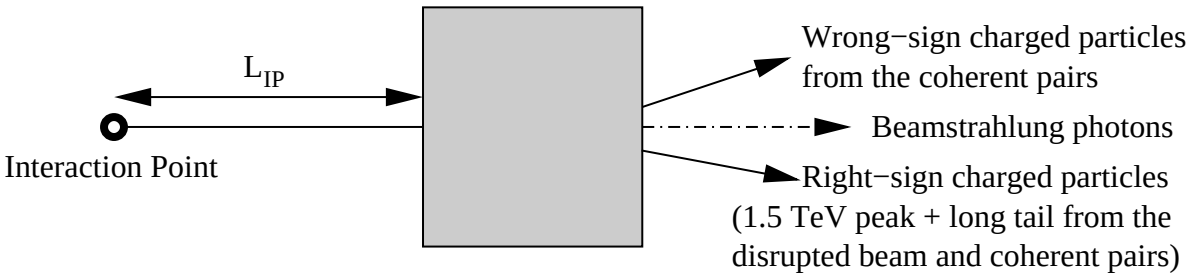

Figure 6: Schematic layout of a CLIC post-collision extraction magnet, which aims at separating the three components of the outgoing beam, while they are still inside a common vacuum pipe.

Beamstrahlung photons are obviously not affected by the presence of the dipole magnet. At its exit, the transverse size of the photon cone only depends on its angular divergence and on the distance $L_{IP} + L_D$ from the interaction point to the dipole end. In the case of ideal collisions, the rms value of the vertical angular divergence of the beamstrahlung photons is 26 μrad. However, it may become much larger if there is a small vertical offset in position and/or angle, which can occur when tuning the machine (when the incoming electron and positron beams are vertically flat, horizontal offsets do not affect the disruption process at the interaction point). GUINEA-PIG simulations suggest that the largest rms value of the vertical angular divergence of the beamstrahlung photons is obtained with a small position offset (about 10 nm) at the interaction point, and that it is about 80 μrad, see Section 5.

The magnetic rigidity of the magnet is:

$$BR \text{ [T.m]} = 3.3356\, p_0 \text{ [GeV/c]}. \tag{6}$$

For particles with a momentum p_0 of 1.5 TeV/c, this leads to:

$$\theta \text{ [mrad]} = 0.2 \times BL_D \text{ [T.m]}. \tag{7}$$

where L_D is the length of the dipole magnet.

Here, the vertical bending angle θ is very small. Therefore, the vertical deviation δy_0 of the 1.5 TeV particles can be written as follows:

$$\delta y_0 = R(1 - \cos\theta) \simeq \frac{L_D \times \theta}{2}. \tag{8}$$

For an excellent separation between the beamstrahlung photons and the high-energy peak of the disrupted beam, the vertical deviation δy_0 at 1.5 TeV must be 10 times larger than the worst rms photon cone size at the exit of the dipole:

$$\theta \text{ [mrad]} = 1.6 \times \left(1 + \frac{L_{IP}}{L_D}\right). \tag{9}$$

By combining equations (7) and (9), one eventually obtains a second-degree equation for L_D, where the magnetic field B (expressed in T) and the distance L_{IP} (expressed in m) enter as two independent parameters:

$$BL_D^2 - 8L_D - 8L_{IP} = 0. \tag{10}$$

This equation has only one physical solution, which is:

$$L_D = \frac{4}{B}\left(1 + \sqrt{1 + L_{IP}B/2}\right). \tag{11}$$

In order to avoid magnetic saturation in the iron, whilst providing a significant bending force, the field strength B should typically be 1 T. As for the distance between the interaction point and the entrance of the extraction magnet, we choose $L_{IP} = 16$ m, which ensures that the dipole is placed outside of the detector. This leads to a magnet length L_D of 16 m, for a vertical bending angle of 3.2 mrad at 1.5 TeV. It does not seem possible to have one single extraction magnet. Instead, one should separate the three components of the outgoing beam in several steps. The design that we propose is based on four extraction dipole magnets, spaced by 1 m, with a field strength of 1 T and a length of 4 m each. The transverse beam sizes must be carefully estimated at the entrance and the exit of each dipole magnet, in order to derive the adequate sizes for the vacuum pipe in the air gaps, and thereby for the magnets themselves. Numerous particle trackings were performed with DIMAD [9] for this purpose. The program computes particle trajectories using the second order matrix formalism [10]. The present version of the code makes sure that the matrix treatment is correct to all orders for energy deviations. By default, every element defined in DIMAD is placed on a reference trajectory that is determined by the nominal beam at 1.5 TeV. When tracking the beamstrahlung photons or the particles of the coherent pairs with the wrong-sign charge, one must introduce a small vertical misalignment for all elements of the post-collision line. Having introduced aperture limitations, the power losses can be estimated using:

$$P_{loss} = 1.602 \times 10^{-10} \frac{N_p\, n\, f}{N_{tracks}} \sum_{i=1}^{N_{loss}} E_i. \tag{12}$$

Here, N_p is the number of particles per bunch, n is the number of bunches per RF pulse, f is the repetition frequency (in Hz), E_i is the energy of the lost particle i (in GeV), N_{tracks} and N_{lost} are respectively the number of tracked and lost particles. With these conventions, P_{loss} is expressed in Watts.

In the horizontal direction, the beam size increases linearly with the distance to the interaction point and the most stringent constraint for the horizontal aperture of the vacuum pipe comes from the coherent pairs, which have the largest horizontal angular divergences (about 0.2 mrad for both electrons and positrons, in the case of ideal e^+e^- collisions).

In the vertical direction, the situation is more complicated, as one must consider the deflection of each particle by the four bending magnets, which depends on their charge and their energy. As the spacing between the beamstrahlung photons and the charged beams increases, so do their vertical sizes, because of the large energy spread of the disrupted beam and the coherent pairs. Indeed, in order to accept all components of the outgoing beam and thereby maintain the power losses below 10 W per magnet, typically, one would have to set the vertical aperture of the vacuum pipe to about 20 cm in the first extraction dipole and at least 3 m in the fourth one, which is obviously not achievable. On the other hand, if Y_{pipe} was set to 20 cm in all magnets, this would lead to power losses of respectively 5, 39 and 94 kW in the second, third and fourth extraction dipole, which is not acceptable either.

One way to keep simultaneously the power losses and the transverse dimensions of the extraction magnets at a reasonable level is to install collimators between them. Their purpose is to absorb some of the particles found in the low-energy tails, which are far away from the reference beam trajectory, thereby preventing them from hitting the coil or the iron yoke of the magnet downstream. In DIMAD, as soon as an electron or positron has $|y - y_0| \geq Y_c$ inside a (rectangular) collimator, it is removed from the list of tracked particles. Here, y_0 refers to the vertical position of the reference charged particle at 1.5 TeV.

In our design, we set the vertical aperture Y_{pipe} to 20, 55, 90 and 125 cm in the first, second, third and fourth extraction magnet, respectively. All of them are centered on the axis of the beamstrahlung photon cone. Also, in order to keep the beam losses below 10 W in each extraction magnet, we propose to install two collimators, with a length of 20 cm each, between them. These two collimators are located 30 cm downstream and upstream of each extraction dipole, respectively. In Table 2, we summarize the values chosen for the vertical half-aperture Y_c, as well as the power losses that are expected in each collimator.

Having derived the optimal value of Y_{pipe} from DIMAD trackings, one should then make sure that the ratio between the transverse apertures of the beam pipe is not too large. Indeed, the rounder the vacuum pipe is, the more uniformly the air pressure is distributed on its outer side. Meanwhile, the horizontal size of the vacuum pipe (and thereby of the gap and the extraction magnet itself) must remain small enough to avoid encumbrance problems, which may result from the presence of the incoming beam line. Therefore, we set X_{pipe} to 12, 15, 18 and 21 cm in the first, second, third and fourth extraction magnet, respectively.

Collimator	Y_c (cm)	Beam losses (kW)
1-2 (a)	7.8	0.04 and 0.02
1-2 (b)	8.0	0.05 and 0.02
2-3 (a)	22.2	0.15 and 0.05
2-3 (b)	21.7	0.16 and 0.04
3-4 (a)	38.8	0.37 and 0.11
3-4 (b)	37.4	0.34 and 0.10

Table 2: Vertical half-apertures (with respect to the associated reference charged beam at 1.5 TeV) for the collimators installed between the extraction magnets, and corresponding power losses for each type of charged beam.

Note that, in order to avoid the vacuum pipe to collapse because of the air pressure on its outer side, it should be elliptical rather than rectangular. In addition, the thickness of the beam pipe wall should be larger along the horizontal axis than along the vertical axis. External reinforcements must also be considered, but they should not require too much space, so that the magnet gap does not become too large. In the following, the thickness T of the beam pipe wall is set to 5 mm along the vertical axis and, for the sake of simplicity, we assume that the ratio between T_x and T_y is more or less the same as between the transverse apertures of the vacuum pipe. A more detailed study of the vacuum constraints and the associated technological solutions is beyond the scope of this paper.

Let us now estimate the transverse dimensions of the excitation coil. For this purpose, we assume that half of its cross section is used for cooling and we use a current density $J = 10$ A/mm^2. Neglecting the contribution of the iron yoke in Ampere's law and using $X_{coil} = g$, we find that:

$$Y_{coil} = \frac{2B}{\mu_0 J} = 15.9 \text{ cm}. \tag{13}$$

When taking into account the constraints of the vacuum pipe thickness, one obtains:

$$h \text{ [cm]} = Y_{pipe} + Y_{coil} + 2T_y = Y_{pipe} + 16.9 \text{ cm}, \tag{14}$$

$$g \text{ [cm]} = X_{pipe} + 2T_x = X_{pipe} + 1 \text{ cm} \times \frac{Y_{pipe}}{X_{pipe}}. \tag{15}$$

The most relevant characteristics of each extraction magnet are given in Table 3. In order to derive the minimum horizontal dimension $2d + g$, we follow the conventions of Figure 5 and we use equation (5) with a maximal field of 1.7 T in the iron yoke. The horizontal spacing between the post-collision line and the incoming beam line (32 cm and 72 cm at the entrance of the first and fourth dipole, respectively) is large enough to allow insertion of all extraction magnets.

Extraction Magnet	g (cm)	h (cm)	nI (kA.turns)	$2d+g$ (cm)
1	13.7	36.9	109.0	35.4
2	18.7	71.9	148.8	61.0
3	23.0	106.9	183.0	85.9
4	27.0	141.9	214.8	110.5

Table 3: Main characteristics of the four extraction magnets installed at the beginning of the CLIC post-collision line.

The vertical beam profiles that are obtained at the exit of the fourth extraction magnet are shown in Figure 7. At this stage, all components of the outgoing beam are still inside the same vacuum pipe.

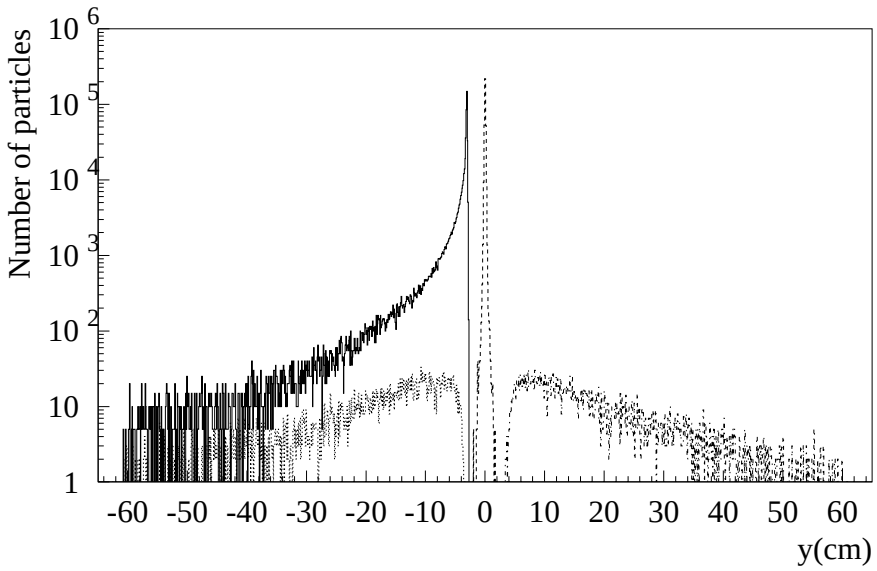

Figure 7: Vertical beam distribution at the exit of the fourth extraction magnet, for the disrupted beam (full line), the beamstrahlung photons (dashed line) and the e^+e^- coherent pairs (dotted and dot-dashed lines).

3.2 Physical separation of the different components of the CLIC outgoing beam

Downstream of the fourth extraction magnet, we physically separate the particles of the coherent pairs which have the wrong-sign charge from the other components of the outgoing beam. A schematic layout of the separation region is shown in Figure 8.

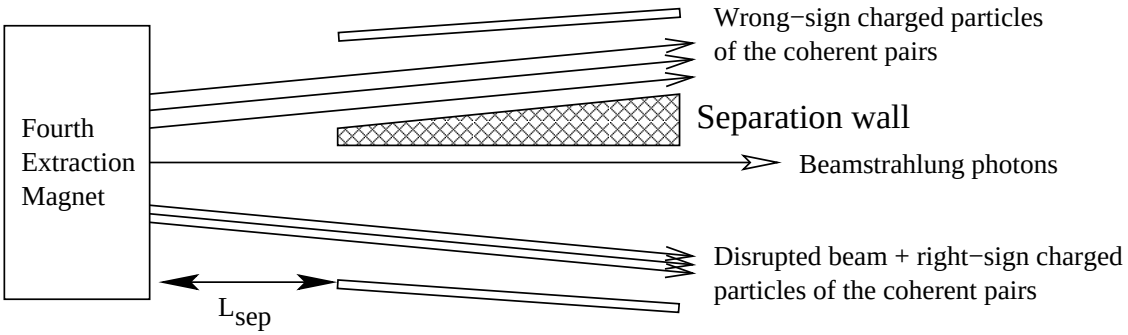

Figure 8: Schematic layout of the separation region, downstream of the fourth extraction dipole magnet.

Synchrotron radiation is emitted by all charged particles inside the extraction magnets. In DIMAD, this effect is taken into account, but it only translates into an energy loss for the particles that are tracked through a magnetic field (the program does not actually generate the corresponding photons). Since the synchrotron radiation is found between the beamstrahlung photon cone and the high-energy edge of the charged beam, it may damage any piece of material used to physically separate the different components of the outgoing beam, in particular the current sheet of a septum magnet. However, the intensity of the synchrotron radiation is much smaller for the particles coming from the coherent pairs than for the disrupted beam. Also, because of their energy spectrum, the coherent pairs are likely to produce a rather wide synchrotron radiation cone, leading thus to a much smaller power loss density than the disrupted beam, for which most of the synchrotron radiation comes from the high-energy peak. Hence, a common vacuum pipe is used for the beamstrahlung photons and the disrupted beam.

The vertical dispersion (and thus the distance between the centre of the beamstrahlung photon cone and the 1.5 TeV reference wrong-sign charged particle of the coherent pairs) depends on the distance L_{sep} to the exit of the fourth extraction dipole:

$$D_y \text{ [cm]} = 3.04 + 0.32 \times L_{sep}. \tag{16}$$

The vertical dispersion D_y must be large enough to allow the insertion of a wall with a thickness of 5 mm where the separation occurs. In addition, we require that the 1.5 TeV reference wrong-sign charged particle of the coherent pairs remains at least 5 mm away from the inner side of its vacuum pipe. Finally, the vertical size of the beamstrahlung photon cone must be taken into account. Its largest rms value $\text{Max}[\sigma_y(\gamma)]$ is obtained with a small position offset at the interaction point and is about 3 mm in the separation region. By requiring the distance between the inner side of the vacuum pipe and the centre of the beamstrahlung photon cone to be $10 \times \text{Max}[\sigma_y(\gamma)]$, we obtain $D_y = 4$ cm, and therefore L_{sep} should be 3 m.

Figure 9 shows the transverse beam profiles, as obtained in the separation region, i.e. 38 m downstream of the interaction point. The stars shows the inner wall of the common vacuum pipe, prior to the separation. It has $X_{pipe} = 21$ cm and $Y_{pipe} = 178$ cm. For the wrong-sign charged particles of the coherent pairs, the vacuum pipe just after separation is elliptical and placed such that the 1.5 TeV reference charged particle is 5 mm away from the lower wall, at $x = 0$. The horizontal and vertical apertures are 15.0 cm and 83.0 cm, respectively. As for the other components of the outgoing beam, the vacuum pipe just after separation consists of two joined half-ellipses. The upper one has its origin at the centre of the beamstrahlung photon cone, and its two semi-axis are $X_{up} = 10$ cm and $Y_{up} = 3$ cm. The lower half-ellipse is centered on the path of the 1.5 TeV reference charged particle of the disrupted beam, with $X_{down} = 10$ cm and $Y_{down} = 84$ cm.

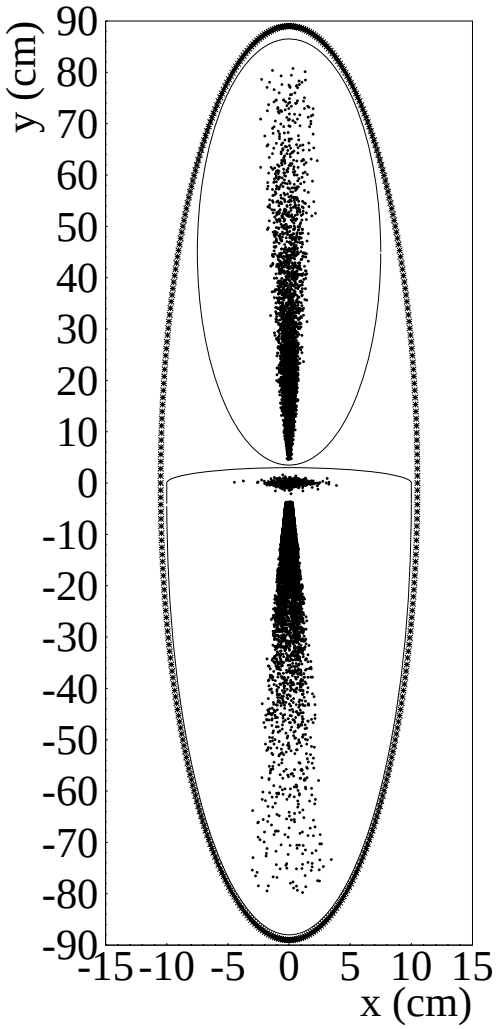

Figure 9: Transverse beam profiles obtained in the separation region, 38 m downstream of the interaction point.

4 Transport to the dump

After having separated the various components of the outgoing beam, one must not only bring them to a dump through a dedicated transport line, but also measure their main properties in order to recover information on the e^+e^- collisions. For this purpose, one has to minimize the beam losses and thus collect as many particles as possible in order to obtain the most accurate image of the outgoing beams when they leave the interaction region. Another constraint that must be taken into account is the dimension of the dump window [12]. If it is circular, with a radius R and a thickness d, the mechanical stress σ_m due to a pressure difference Δp is given by:

$$\sigma_m = 0.49\,\Delta p \times \left(\frac{R}{d}\right)^2. \tag{17}$$

When choosing the material of the dump window, one must also take into account the cyclic thermal stress σ_c. It is due to the rapid heating of the material during the passage of a bunch train with $n\,N_b$ particles. One must make sure that d remains significantly smaller than one radiation length. In that case, only ionization losses occur in the dump window. The instantaneous temperature rise at the centre of the beam distribution is given by:

$$\Delta T_{inst} = \left(\frac{dE}{\rho dx}\right) \times \frac{n\,N_b}{2\pi C \sigma^2_{beam}}, \tag{18}$$

and the corresponding cyclic thermal stress is:

$$\sigma_c = \frac{1}{2}\alpha E \Delta T_{inst}. \tag{19}$$

Here, α is the thermal expansion coefficient and E is the elastic modulus of the chosen material. When calculating ΔT_{inst}, the only relevant parameter is the heat capacity C, since $(dE/\rho dx)$ does not significantly depend on the material. The most severe thermal stress is caused by the non-colliding charged beam at 1.5 TeV (with a failure of every magnet along its path), or by the beamstrahlung photon cone in the case of ideal e^+e^- collisions, for which σ_{beam} is the smallest. A detailed design of the CLIC dump window is beyond the scope of this study. However, some constraints are highly relevant for the design of the transport line between the separation region and the dump. For instance, σ^2_{beam} should be larger than 1 mm^2 for the non-colliding beams or the beamstrahlung photons. Also, the R/d ratio of the dump window, and thereby the transverse apertures of the vacuum pipe for a given thickness d, must remain low enough to avoid a too large mechanical stress.

In the following, we choose to use the same dump for the main charged beam and the beamstrahlung photons. It should be located about 250 m downstream of the interaction point. In that case, the transverse sizes $\sigma_x(e^\pm)$ and $\sigma_y(e^\pm)$ of the non-colliding beam at the dump window are 0.94 mm and 1.22 mm, respectively (without any magnetic field along their path). As for the beamstrahlung photons, we find $\sigma_x(\gamma) = 8.2$ mm and $\sigma_y(\gamma) = 6.5$ mm, in the case of ideal e^+e^- collisions. On the other hand, a separate dump is needed for the wrong-sign charged particles of the coherent pairs.

4.1 Collection and analysis of the coherent pairs

In order to recover information on the coherent pairs, only the particles with the wrong-sign charge can be used, since the other ones can not be distinguished from the low-energy tail of the disrupted beam. Therefore, it is crucial to collect as much particles as possible, in order to then derive the full energy spectrum of the coherent pairs from the vertical beam profile of the particles with the wrong-sign charge. Those with an energy deviation δ larger than -0.95 (i.e. with $E \geq 75$ GeV) are generally present just after the separation region. However, because of the vertical dispersion and its non-zero derivative D'_y, the size of the wrong-sign charged beam rapidly increases, and so does the vertical aperture of the beam pipe if one wants to keep all particles inside it. On the other hand, one must eventually decrease the transverse dimensions of the vacuum pipe, in order to obtain a reasonable value for the radius of the dump window.

An early measurement of the beam profiles is therefore necessary. The left-hand side plot of Figure 10 shows the correlation between the vertical position and the energy for the particles of the coherent pairs with the wrong-sign charge just after the separation region, i.e. 38 m downstream of the interaction point (these particles were generated with $x = y = 0$ and $x' = y' = 0$). On the right-hand side plot, a comparison between the energy spectrum derived from the vertical beam profile and the true one is presented: a good agreement is obtained and almost the whole energy distribution of the coherent pairs can be retrieved with this method.

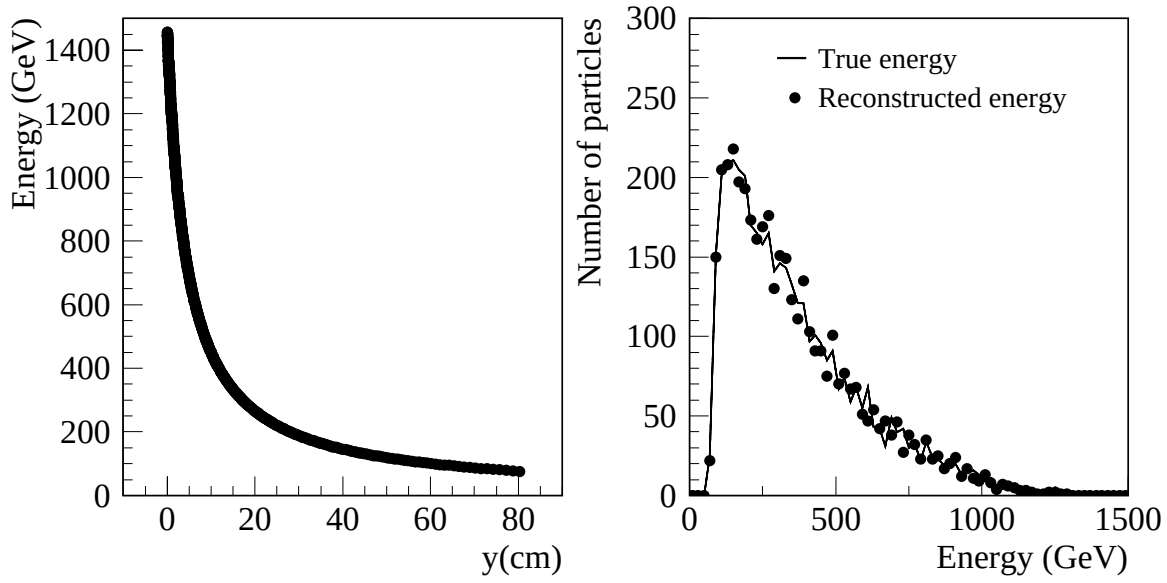

Figure 10: Reconstruction of the energy spectrum of the coherent pairs from the vertical beam profile of the wrong-sign charged particles just after the separation region, see text for details.

After the separation region, the vertical aperture of the vacuum pipe remains equal to 83 cm over a distance of 1 m in order to allow a measurement of the transverse beam profiles. Downstream, Y_{pipe} is decreased to 20 cm, which inevitably leads to losses. The effective thickness of the vacuum pipe wall strongly depends on the angle of incidence of the particles passing through it. In order to ensure that only ionization losses occur in the vacuum pipe, its effective thickness should not exceed 1 cm. Hence, small angles of incidence must be avoided. For this purpose, the reduction of Y_{pipe} must be performed over a short distance, which is 1.26 m in our design. Because the beam intensity of the coherent pairs is relatively low, we do not expect the corresponding cyclic thermal stress to be a significant limitation. We propose the following set-up in order to derive useful information from the detection of the lost particles. A layer of active material should be installed around the vacuum pipe (especially over it), which detects the flux of lost particles along the transport line. After passing through this active layer, the wrong-sign charged particles of the coherent pairs are stopped in a dump, which can be instrumented for measurement purposes, see Figure 11. A more detailed design of the active layer, the dump and its instrumentation is beyond the scope of this paper. Here, we only focus on the tracking of the wrong-sign charged particles of the coherent pairs until they pass through the vacuum pipe and on the relevant information that can be retrieved from the beam loss distribution.

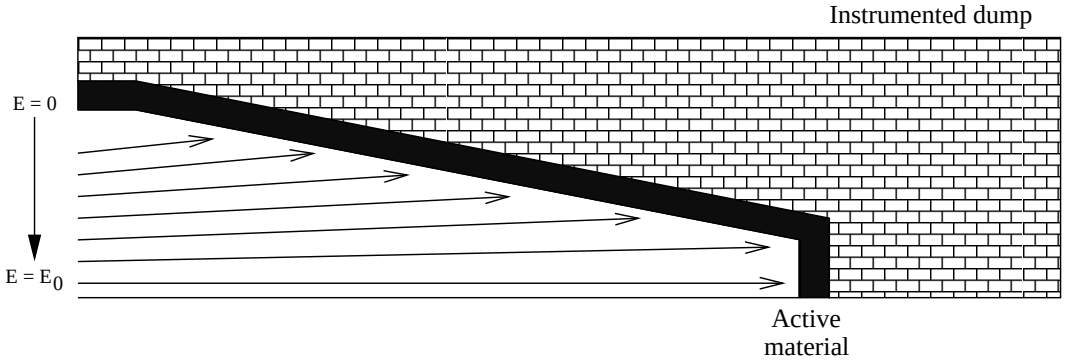

Figure 11: Schematic layout of the transport line between the exit of the separation region and the dump window, for the particles of the coherent pairs with the wrong-sign charge.

The wrong-sign charged particles of the coherent pairs that have an energy larger than 300 GeV reach the dump window. The corresponding beam power is 30.9 kW, i.e. about 75% of the beam power at the exit of the separation region. The other particles are lost along the transport line, upstream of the dump window, as shown in Figure 12. Therefore, most of the low-energy peak in the energy spectrum of the coherent pairs can be retrieved by measuring the flow of lost particles as a function of their position of loss along the transport line, which allows a direct determination of their energy.

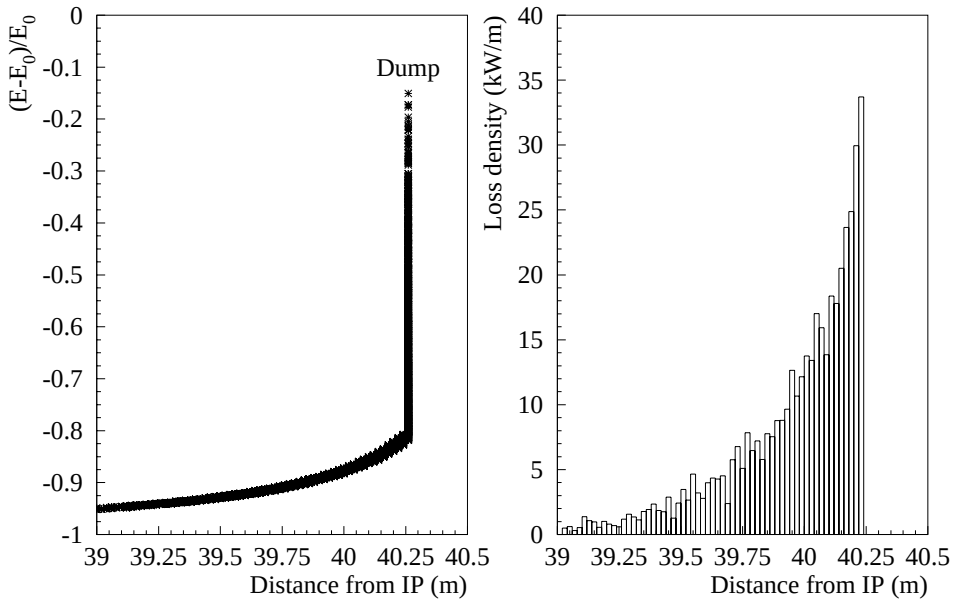

Figure 12: Relative energy spread of the lost particles of the coherent pairs with the wrong-sign charge, as a function of their position of loss in the CLIC post-collision line (left) and power loss density in the transport line downstream of the separation region (right). Only a small fraction of the power is actually deposited in the wall of the vacuum pipe.

4.2 Collection and analysis of the disrupted beam and of the beamstrahlung photons

The method used to rapidly collect the wrong-sign charged particles of the coherent pairs after the separation region can not be used for the transport line of the other (main) charged beam. Indeed, one needs the dump window to be far enough from the interaction point (250 m typically), so that the transverse sizes of the non-colliding beam become larger than 1 mm. On the other hand, such a long drifting space without any magnetic element between the separation region and the dump is not a solution either, because this would rapidly lead to an extremely large disrupted beam. Hence, the bend provided by the four extraction magnets should be followed by a bend in the opposite direction, in order to eventually have $D'_y = 0$ at the exit of the vertical chicane (and at the beam dump). For this purpose, we propose to use four C-type dipole magnets. A schematic layout of the transport line for the disrupted beam is shown in Figure 13. In our design, the C-type magnets are placed after the dump of the wrong-sign charged particles of the coherent pairs, in order to avoid encumbrance problems. Indeed, one needs to have some free space above the iron yoke for the installation of excitation coils, as suggested by Figure 14.

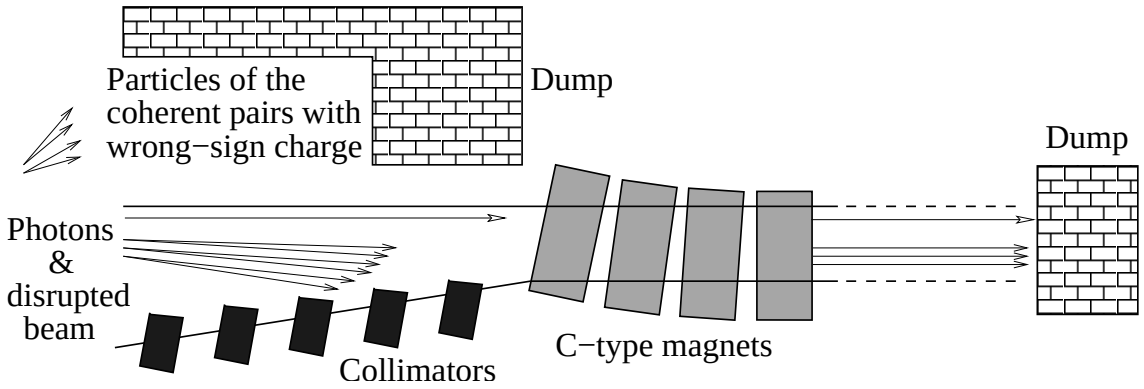

Figure 13: Schematic layout of the second part of the vertical chicane, which bends back the disrupted beam and the particles of the coherent pairs with the same charge, ensuring that D'_y vanishes at the exit of the last C-type magnet.

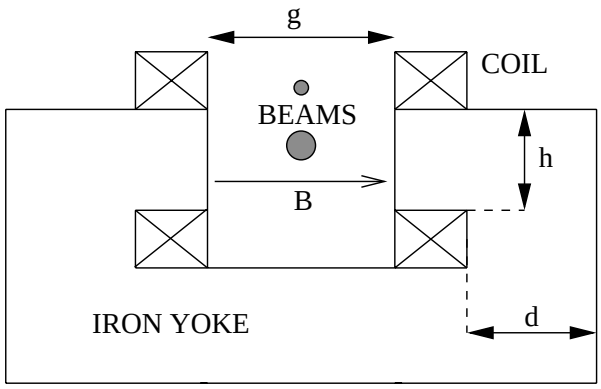

Figure 14: Cross section of a C-type dipole magnet, with the relevant parameters to be considered for its design. The beamstrahlung photons travel between the upper coils, while the disrupted beam passes between the poles.

The first section of the transport line, which starts 38 m downstream of the interaction point, is 10 m long. There, the vertical dispersion grows from 4.0 cm to 7.2 cm, the spacing between the centre of the beamstrahlung photon cone and the upper wall of the vacuum pipe is increased from 3 cm to 6 cm, and the distance between the 1.5 TeV reference charged particle of the disrupted beam and the lower wall of the vacuum pipe is decreased from 84 cm to 64 cm. This aperture reduction inevitably leads to beam losses. Indeed, the charged particles with $\delta \leq 0.85$ do not reach the first C-type dipole magnet. Since their angle of incidence with respect to the surface of the vacuum pipe is usually small, these lost particles interact with a significant amount of matter when passing through the wall of the vacuum pipe and can therefore severely damage it. Five collimators, with a length of 1 m each, are placed along the first 10 m of the transport line, in order to absorb the particles that would not reach the C-type magnets. Two

consecutive collimators are spaced by 1 m. The first one starts 38.5 m downstream of the interaction point and the fifth one ends 0.5 m upstream of the first C-type magnet. Furthermore, while the low-energy particles are absorbed by the five collimators, it is possible to decrease the horizontal aperture of the vacuum pipe from 20 cm to 16 cm without additional beam loss. Figure 9 indeed suggests that the largest values of the horizontal rms beam size are obtained far away from the high-energy peak. A summary of the transverse apertures of the five collimators and of the corresponding power losses is given in Table 4.

Collimator	Y_c (cm)	P_{loss} (kW)
Coll-C1	48.0	6.97
Coll-C2	43.5	7.18
Coll-C3	42.1	7.45
Coll-C4	41.5	7.93
Coll-C5	41.0	8.60

Table 4: Vertical half-apertures (with respect to the 1.5 TeV reference charged beam) for the five collimators placed upstream of the C-type magnets, and corresponding power losses for the disrupted beam and the particles of the coherent pairs with the same charge.

Let us now focus on the four C-type dipole magnets. Each of them is 4 m long and two consecutive magnets are spaced by 1 m. If we set the magnetic field to 1 T in the four C-type magnets, then the vertical dispersion at the exit of the post-collision chicane (67 m downstream of the interaction point) is 10.2 cm for the 1.5 TeV reference particle of the disrupted beam, with $D'_y = 0$. However, because of the emission of synchrotron radiation in the eight magnets of the post-collision chicane, the high-energy peak of the disrupted beam has $\delta = -0.06$ at the exit of the last C-type magnet and it is therefore slightly displaced. Furthermore, since D'_y is not exactly zero for the high-energy peak of the disrupted beam, it leaves the post-collision chicane with a small positive angle. One way to compensate for this effect is to slightly reduce the field strength to 0.973 T in the four C-type magnets. In that case, particle trackings with DIMAD suggest that the high-energy peak (with $\delta = -0.06$) leaves the chicane with a vertical angle of 0.086 mrad with respect to the 1.5 TeV reference charged particle of the disrupted beam. However, for the reference particle itself, one finds that $D'_y = 0.086$ mrad. This means that, when using the new C-type magnet settings, the high-energy peak at 1.4 TeV is parallel to the beamstrahlung photon cone, 10.4 cm away from its centre.

Figure 15 shows the y and y' distributions of the disrupted beam after the last C-type magnet, as a function of the energy. The particles found in the core of the high-energy peak at $y = 0$ leave the post-collision chicane parallel to the beamstrahlung photons, i.e. with $y' = 0$.

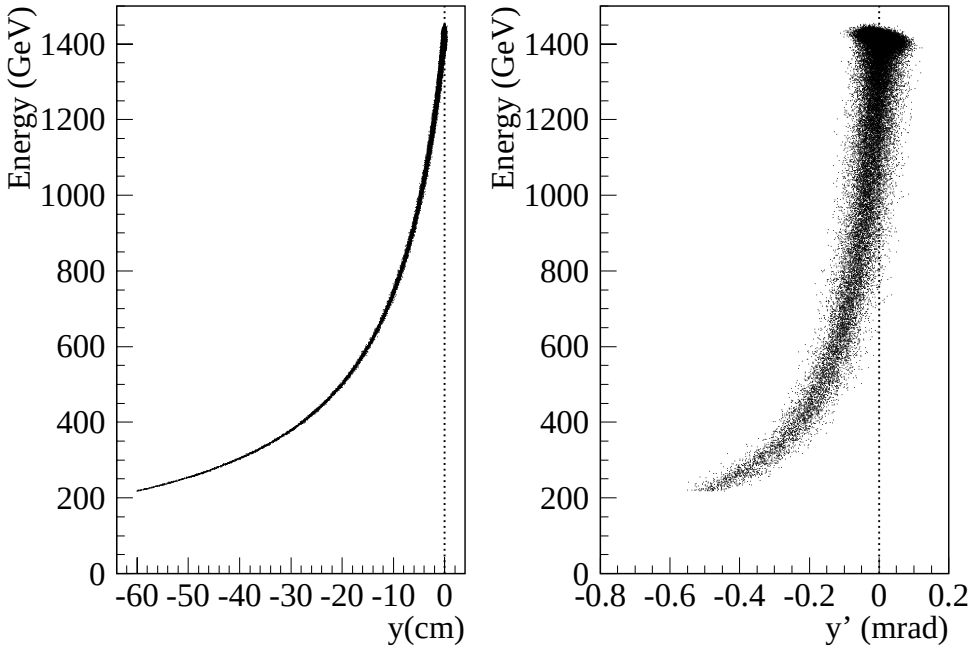

Figure 15: y and y' distributions as a function of the energy for the disrupted beam, as obtained at the exit of the post-collision chicane.

If the gap of the C-type magnets is 20 cm, then an excitation current of 160 kA.turns is required in order to produce a field of 1 T in the gap. This leads to a cross section of 320 cm^2 for the coils, if we assume that half of it is used for cooling and that the current density is 10 A/mm^2. The horizontal dimension of the C-type magnet is $g+2(d+X_{coil})$, where the distance d must be large enough to allow the magnetic flux Φ to fully return through the iron yoke. It is rather trivial to analytically calculate Φ in the lateral parts of the magnet, where the iron yoke is thinest. On the other hand, since the magnetic field is not fully contained inside the gap, it is more complicated to estimate Φ there. The leakage of the flux depends on several parameters, such as the distance between the poles, their shape, the position of the coils, the grade of saturation, etc. There is no simple analytic formula taking into consideration all these aspects. Let us instead consider an ideal configuration, in which the coils are close to the iron, the magnet is not saturated, the flux is entering and leaving the yoke through the (parallel) pole faces only and the distance between the poles is small compared to their width. In that case, about 95% of the flux is contained in $B \times \ell \times (h + 0.5g)$, where ℓ is the length of the C-type magnet. If the maximal field strength inside the iron yoke is B_{max} (chosen to be 1.7 T as in the case of the four window-frame magnets), then the distance d is roughly constrained by:

$$d \geq \frac{B}{B_{max}} (h + 0.5g). \tag{20}$$

With $g = 20$ cm and $h = 65$ cm, the smallest value of d is 43 cm. If the horizontal and vertical sizes of the excitation coils are set to respectively 10 cm and 32 cm, then the minimum horizontal dimension of the C-type magnets is 126 cm. The spacing between the post-collision line and the incoming beam line is 102 cm at the entrance of the first C-type magnet, which is enough to allow its insertion. Downstream, the encumbrance constraints are less severe, since the beam lines are further apart, whilst the transverse dimensions of all four C-type magnets are the same.

Following the vertical chicane, the disrupted beam and the beamstrahlung photons are brought to a common dump, which is located 180 m downstream. If a separation wall was inserted between these two beams, it could be damaged by some particles of the high-energy peak and/or photons, which are in the tail of the y' distributions. We thus propose to transport all particles in the same vacuum pipe, from the exit of the chicane to the dump. Its transverse cross section consists of two joined half-ellipses. At the exit of the chicane, the distance between their origins is 10.4 cm, the (common) horizontal semi-axis X_0 is 8 cm, while the upper and lower vertical semi-axis, Y_{up} and Y_{down}, are respectively 6 cm and 64 cm. If one kept the same geometry until the dump window, then the power losses would be 120 W for the beamstrahlung photons, and 21 kW for the disrupted beam and the particles of the coherent pairs with the same charge.

One should reduce the losses, without significantly increasing the transverse apertures of the vacuum pipe and thereby the size of the dump window, which could then yield a too large mechanical stress. One solution is to bend back the low-energy particles which are far away from the high-energy peak, with $y' < 0$. Meanwhile, the core of the charged beam should remain unaffected. For this purpose, we use vertically focusing quadrupoles centered on the path of the high-energy peak of the disrupted beam. One major constrain for their design is the transverse dimensions of the vacuum pipe, which sets a lower limit on the aperture radius a and thereby on the size of the quadrupoles. As a rule of thumb, the extension of the poles perpendicularly to the beam axis should be roughly $\sqrt{2} \times a$ in order to get a reasonable field quality in the quadrupole and, in addition, the thickness of the return yoke should be at least one half of the pole width [13]. An aperture radius of the order of 70 cm yields a quadrupole width of at least 4 m. Hence, the refocusing quadrupoles must be placed in a region where the horizontal spacing between the incoming and post-collision beam lines exceeds 3 m, i.e. at least 150 m downstream of the interaction point.

Along the 83 m long drift from the exit of the chicane to the first quadrupole, the shape of the vacuum pipe is smoothly modified in order to gain acceptance, in particular for the lower half-ellipse. Its origin is gradually moved away from the path of the high-energy peak by 40 cm (in order to significantly enhance the horizontal aperture seen by the low-energy particles), while the vertical semi-axis is decreased from 64 cm to 28 cm. Doing so, the total vertical aperture of the vacuum pipe grows by 4 cm only. Meanwhile, the horizontal aperture X_0 is increased from 16 to 20 cm.

In our design, the vertically refocusing region consists of 16 quadrupoles, with a length of 2 m and a pole field of 1 T each. Their aperture radius is 70 cm, so the gradient is 1.4 T/m. Two consecutive quadrupoles are spaced by 1 m, the first one being installed 150 m downstream of the interaction point. Figure 16 shows the y and y' distributions of the disrupted beam as a function of the energy, at the exit of the last quadrupole (197 m downstream of the interaction point). The particles found in the high-energy peak at $y = 0$ are still parallel to the beamstrahlung photons, while the particles with less than 800 GeV now have a small and positive y'.

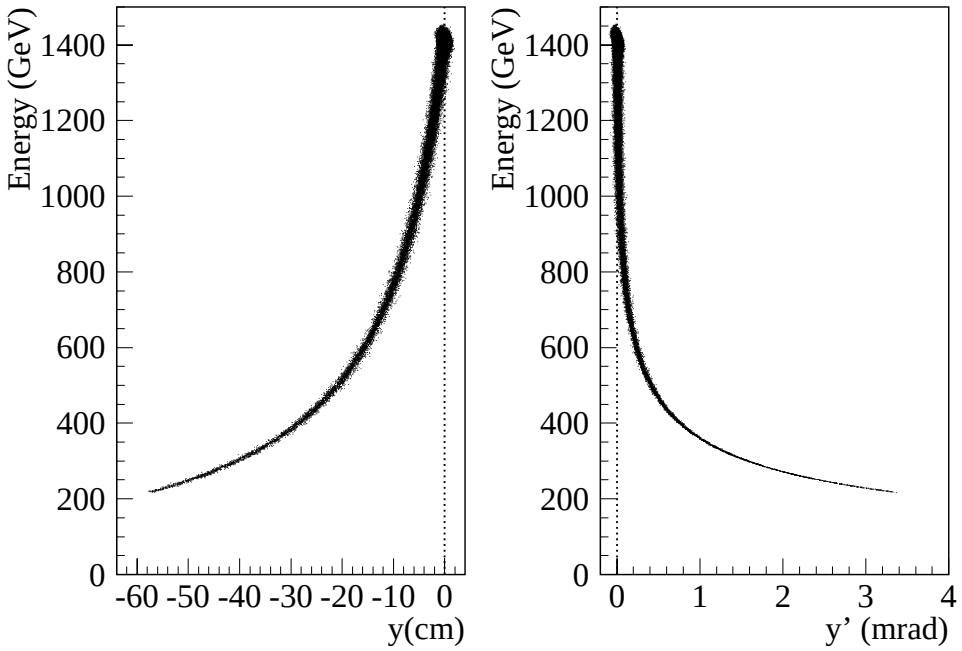

Figure 16: y and y' distributions as a function of the energy for the disrupted beam, as obtained at the exit of the vertically refocusing region.

If the shape of the vacuum pipe wall remains unchanged along the refocusing region, no significant beam loss is expected there. Downstream, in order to ensure a loss free transport of the charged beams, the horizontal aperture of the vacuum pipe must be smoothly increased from 20 cm at the exit of the last quadrupole to at least 26 cm at the dump, located 50 m away. There, the distance between the high-energy peak of the disrupted beam and the inner wall of the vacuum pipe below must exceed 45 cm, which is about 20 cm less than without refocusing. Figure 17 compares the transverse beam distributions at the dump window, with and without the vertical refocusing. Its effect is clearly visible in the right-hand side plot: the low-energy tail becomes significantly shorter in the presence of focusing elements. On the other hand, no significant difference is observed for both the horizontal beam distribution and the high-energy peak in the vertical beam distribution, as expected.

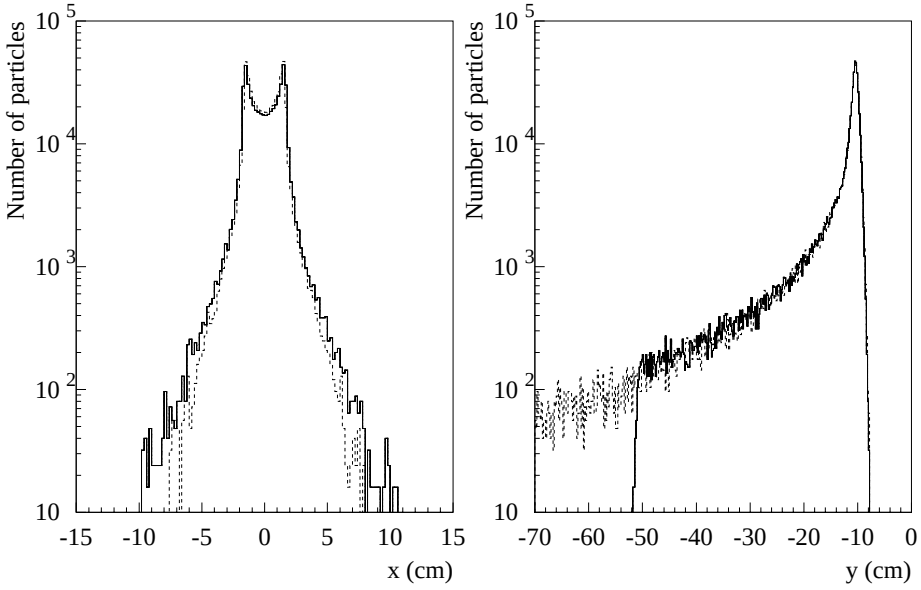

Figure 17: Horizontal and vertical profiles of the disrupted beam and the particles of the coherent pairs with the same charge, at the end of the CLIC post-collision line: the full (respectively dashed) line spectra are obtained with (respectively without) vertically focusing elements downstream of the chicane. At first order, the horizontal beam profile gives an image of the x' distribution at the interaction point, while the vertical beam profile shows the energy spectrum of the disrupted beam.

If no magnetic element was installed downstream of the chicane, then the vertical size of the dump window (and thereby the mechanical stress) would increase with the overall length of the post-collision line. Thanks to the presence of the focusing quadrupoles, the vertical beam size now decreases along the last section of the post-collision line, so the dump window can be made even smaller by extending the last drifting section beyond 50 m (on the other hand, since the horizontal beam size grows, the aperture X_0 should be slightly increased). Note that this configuration allows some flexibility for the design of the final section of the post-collision line. For instance, if fewer quadrupoles are installed or if their focusing strength is weaker, then one only has to move the dump further away in order to keep the same window size and thus the same level of mechanical stress. In addition, if one reduces the transverse dimensions of the quadrupoles (for instance by using the superconducting technology for their design), then it becomes possible to move the refocusing region upstream and, since the length of the drift space between the last quadrupole and the dump becomes longer, one may reduce the number of quadrupoles or their focusing strength without any significant change for the dump window.

Finally, let us discuss the transport of the beamstrahlung photons. After the chicane, the horizontal and vertical semi-axis of the upper (elliptical) part of the vacuum pipe are linearly increased until the dump window, where $\sigma_x(\gamma) = 8.2$ mm and $\sigma_y(\gamma) = 6.5$ mm. The horizontal semi-axis X_0 of the upper half-ellipse is 13 cm, i.e. 16 times larger than $\sigma_x(\gamma)$. As for the vertical semi-axis Y_{up}, it must be large enough to allow a loss free transport of the beamstrahlung photons, but one must also keep in mind that the larger Y_{up}, the larger the cross section of the dump window and, thereby, the mechanical stress. Here, we choose $Y_{up} = 12$ cm, which is 18 times larger than $\sigma_y(\gamma)$. This is also 6 times larger than the worst rms vertical size of the beamstrahlung photon cone at the dump window, which can reach almost 2 cm when there is a small vertical beam-to-beam offset at the interaction point.

Figure 18 shows the transverse beam profiles at the dump window, 50 m downstream of the last quadrupole. The inner wall of the vacuum pipe again consists of two joined half-ellipses. For both of them, the horizontal and vertical semi-axis are respectively 13 cm and 12 cm. The upper half-ellipse is centered on the beamstrahlung photon cone, while the lower one has its origin 50 cm below (like at the exit of the entrance of the refocusing region). The area of the dump window is thus 0.18 m^2, which is about twice less than for the 60 cm diameter dump window of the Large Hadron Collider [14].

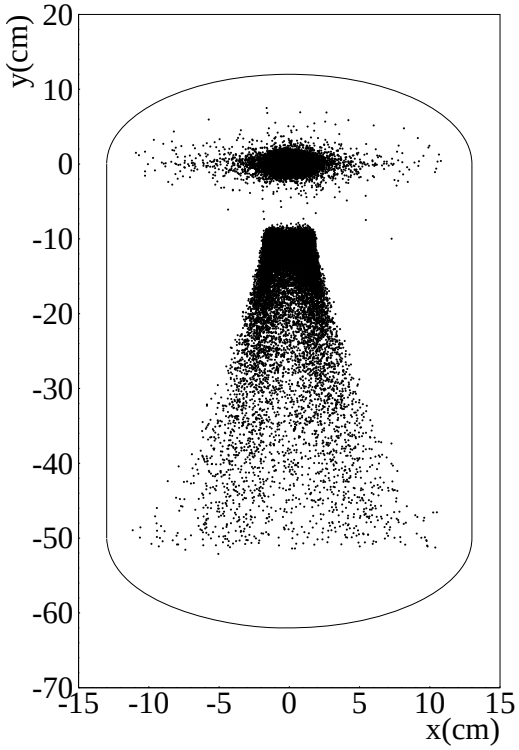

Figure 18: Transverse beam profiles obtained at the dump window, 247 m downstream of the interaction point.

In order to retrieve information on the e^+e^- collisions, one should analyse the transverse distributions of the disrupted beam and the beamstrahlung photons. A detailed design of the instrumentation in the CLIC post-collision line will have to be performed in future studies. At the dump, the beam profile measurements could be achieved by monitoring the temperature distribution in the window or in a laminar sheet of water flowing close to it, for instance with an interferometric thermometer [15]. This signal is related to the energy deposition in the dump window and thus provides information on the angular divergences and the energy spectrum of the outgoing beams.

5 Performance of the CLIC post-collision line with a beam-to-beam offset at the interaction point

The observation and analysis of each outgoing beam will be mandatory during the tuning of the CLIC machine. At that stage, small offsets between the colliding beams will occur, which can strongly affect the beam distributions at the interaction point, and therefore the signals collected along the post-collision line and at the dumps. Since the incoming beams are vertically flat, horizontal offsets do not affect the disruption process. On the other hand, beam-beam effects may be significantly enhanced when a vertical offset is introduced. Figure 19 shows how the beamstrahlung parameter, as well as the number of photons and coherent pairs, vary with a vertical offset in position, but also in angle, at the interaction point. Figures 20 to 23 then show how the x' and y' distributions of the disrupted beam, the beamstrahlung photons and the coherent pairs are affected.

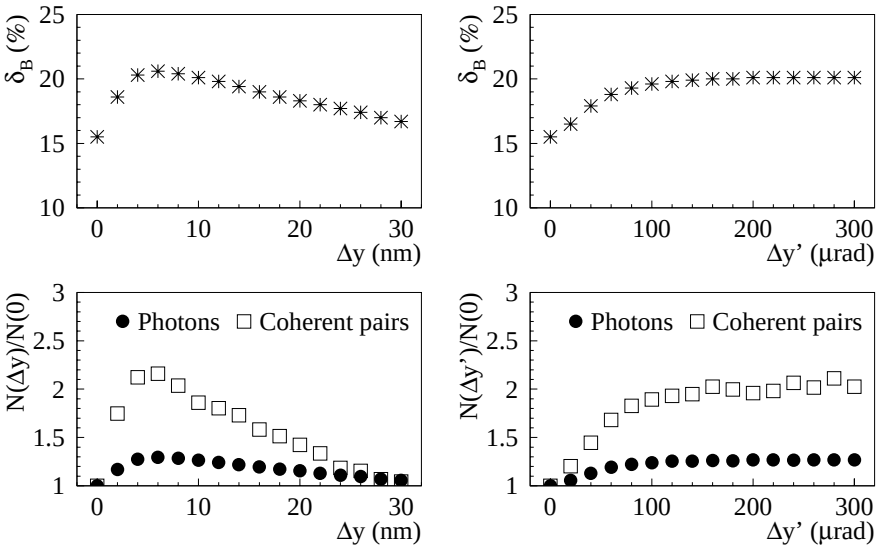

Figure 19: Beamstrahlung parameter δ_B, number of photons and of coherent pairs, as a function of a vertical offset in position or angle at the interaction point.

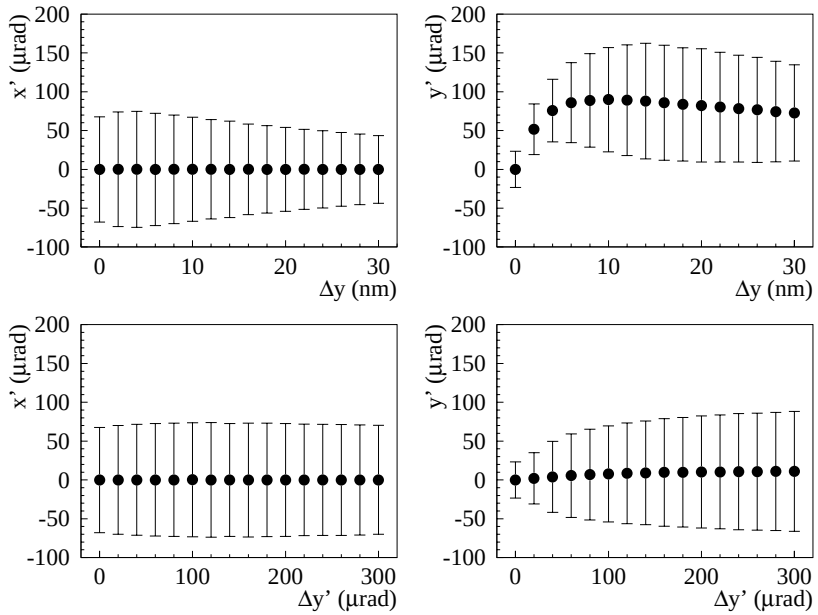

Figure 20: Mean and rms values (full circles and error bars) for the x' and y' distributions of the disrupted beam, as a function of a vertical offset in position or angle at the interaction point.

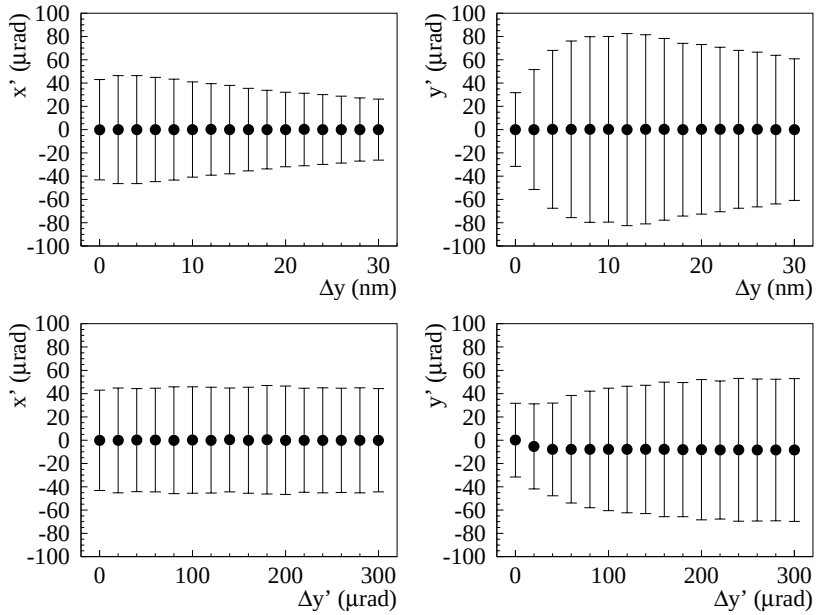

Figure 21: Same as Figure 20, but for the beamstrahlung photons.

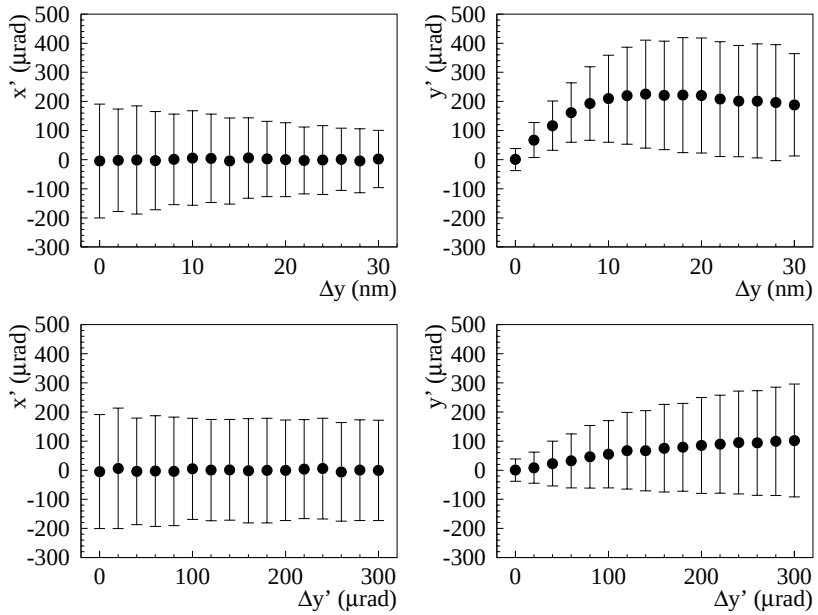

Figure 22: Same as Figure 20, but for the particles of the coherent pairs with the right-sign charge.

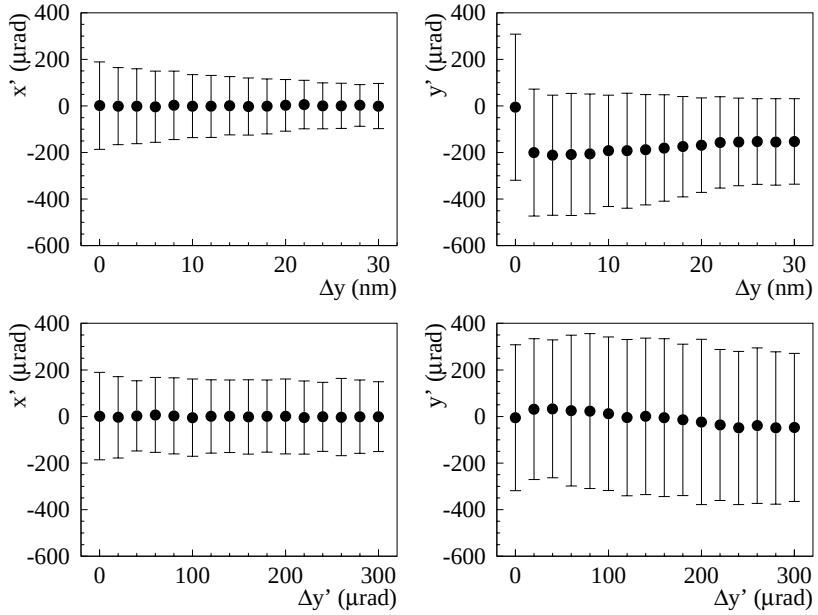

Figure 23: Same as Figure 20, but for the particles of the coherent pairs with the wrong-sign charge.

For relatively small position offsets, the electromagnetic field seen by the bulk of charged particles in one incoming beam increases with the distance to the other beam. So does the disruption and, in turn, the emission of beamstrahlung photons and coherent pairs. For larger position offsets, the field seen by each bunch becomes smaller and smaller as the distance between the incoming beams increases. The strongest beam-beam effects are obtained when $\Delta y \simeq 10$ nm. Each incoming beam receives a vertical kick towards the other beam when passing through its strong electromagnetic field. As a result, the y' distribution of the disrupted beam gets not only a large rms value, but also a non-zero mean value. The same conclusion is true for the coherent pairs. The particles that have the same charge as the disrupted beam receive a vertical kick in the same direction, but with a larger amplitude, because their energy is lower. For the particles of the coherent pairs with the wrong-sign charge, the kick is in the opposite direction. Since the beamstrahlung photons do not carry any electric charge, the mean value of their y' distribution remains equal to zero, but the associated rms value is significantly larger than in the case of ideal collisions. In the upper plots of Figures 20 to 23, we have only considered the outgoing beam that receives a positive vertical kick (i.e. upwards). For the other beam, the mean values of the y' distributions have the opposite sign, while the rms values are unchanged. With an angular offset at the interaction point, both outgoing beams have the same transverse distributions. In the lower plots of Figures 20 to 23, we have only shown the results obtained with a positive $\Delta y'$ in GUINEA-PIG. If the angular offset was negative, the mean values of the y' distributions would have the opposite sign, while the rms values would remain the same.

So far, we have discussed the design of one CLIC post-collision line only, in which the disrupted beam is deflected downwards by the vertical chicane. In the following, this will be the case for the other post-collision line as well. Consequently, since the mean values of the y' distributions of the two disrupted beams (and of the e^+e^- coherent pairs) have opposite signs in the presence of a vertical offset in position at the interaction point, the power losses may not be exactly the same in the two post-collision lines. On the other hand, if the offset only affects the vertical crossing angle of the incoming beams, then the beam transport can be analyzed in the same way for both post-collision lines. This is illustrated by Figure 24.

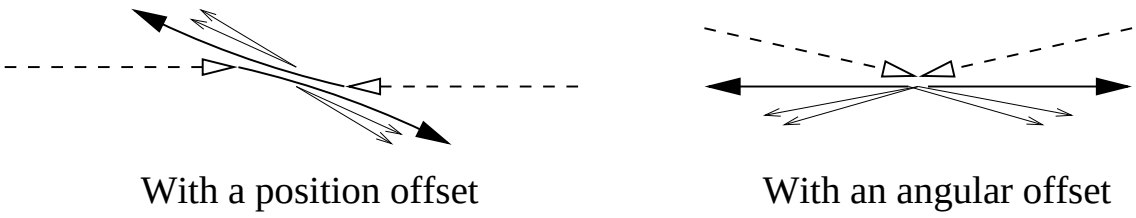

Figure 24: Deflection of the beams during the bunch crossing, with a vertical offset in position or angle at the interaction point.

5.1 Performance of the CLIC post-collision line with a vertical position offset at the interaction point

Let us first discuss the influence of a non-zero Δy on the beam losses upstream of the separation region. The power deposited by the charged beams in each extraction magnet does not exceed 40 W: most of the additional losses occur in the collimators between them. For the disrupted beam, the power losses per collimator reach 200 W between the first and the second magnets. For each collimator located between the second and the third magnets, the losses can go up to 400 W. Finally, the collimators placed between the third and the fourth magnets may receive up to 900 W each. For each type of particles in the coherent pairs, these numbers become respectively 150 W, 200 W and 350 W. The largest losses are obtained for small values of Δy (less than 10 nm). There are two major reasons for the increase of the power losses, as compared to the case of ideal e^+e^- collisions: a non-zero mean value for the y' distribution of the charged beams and a larger amount of low-energy particles. However, the effect of the vertical kick during the bunch crossing (which affects the losses in the two post-collision lines in a slightly different way) becomes negligible as soon as the bending angle provided by the extraction magnets is much larger than the deflection during the bunch crossing, which is usually the case after the second extraction magnet. Downstream, the additional losses are mostly determined by the amount of low-energy particles.

Downstream of the separation region, we first focus on the particles of the coherent pairs with the wrong-sign charge. The left-hand side plot of Figure 25 shows how the beam power passing through the dump window varies with Δy. The right-hand side plot indicates that the fraction of the beam power reaching the dump does not significantly depend on Δy and is about 75%.

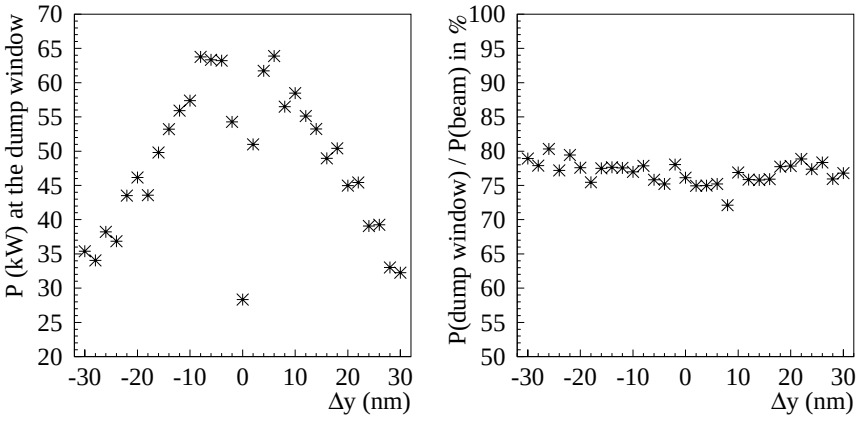

Figure 25: Beam power passing through the dump window of the extraction line of the wrong-sign charged particles of the coherent pairs, as a function of the vertical position offset at the interaction point.

Here, we have used positive and negative values of the vertical position offsets in order to distinguish between the two post-collision lines. But, our results do not suggest any significant difference between them. Indeed, the transverse distributions of the coherent pairs downstream of the four extraction magnets are mostly determined by the energy spread. Hence, the small vertical kicks occuring during the bunch crossing do not have any sizeable effect. By a combined measurement of the beam power passing through the dump window (which is about 75% of the total beam power) and of the energy spectrum, one can determine the amount of coherent pairs for any given position offset at the interaction point.

We now focus on the disrupted beam and the particles of the coherent pairs with the same charge. Just downstream of the separation region, the low-energy particles (with $\delta < -0.85$ typically) are absorbed in five collimators. Since a small vertical position offset at the interaction point leads to an enhancement of the disruption process and of the production of coherent pairs, a larger amount of low-energy particles deposit their energy in the collimators when $\Delta y \neq 0$, see Figure 26. Again, we use positive and negative values of Δy in order to distinguish between the two post-collision lines, but no significant difference is observed, since the vertical beam profiles are dominated by the contribution of the energy spread. In addition, as in the case of ideal e^+e^- collisions, a loss free transport of the disrupted beam through the four C-type magnets downstream is possible thanks to the presence of the collimators.

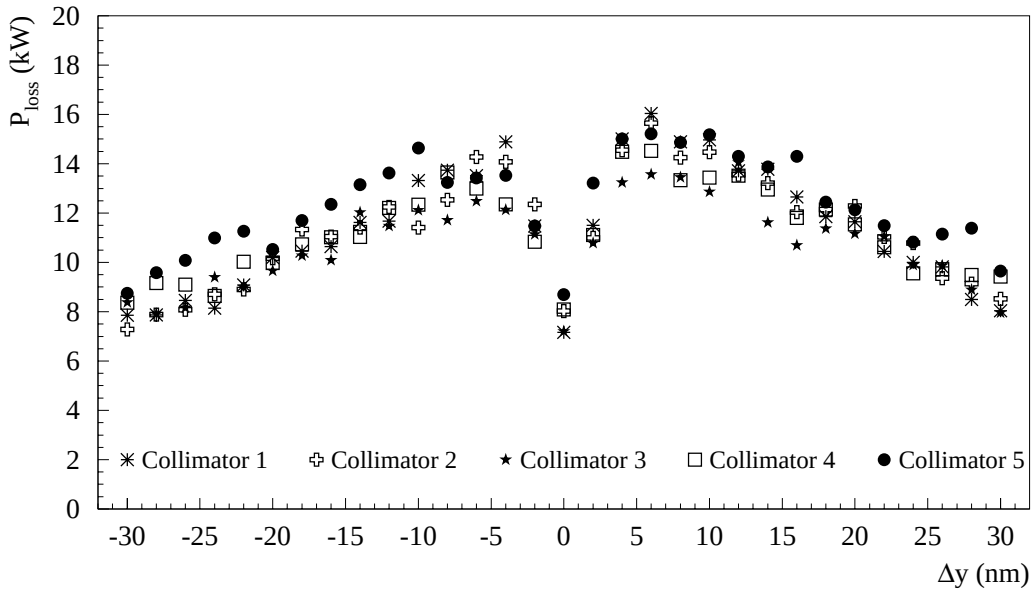

Figure 26: Power losses in the collimators placed at the beginning of the transport line for the disrupted beam and the same-sign charged particles of the coherent pairs, as a function of the vertical offset in position at the interaction point.

If there is a small vertical position offset at the interaction point, all particles receive a small kick during the bunch crossing, which can be measured at the exit of the chicane, where $D'_y = 0$ for the high-energy peak. For this purpose, one needs to experimentally determine the vertical position offset and angle of the disrupted beam when it leaves the fourth C-type magnet. This can easily be done by using beam monitors in order to reconstruct the (straight) beam path between the chicane and the quadrupoles. Figure 27 shows how these quantities vary with Δy. Note that they have opposite signs in the two post-collision lines. The vertical displacement of the high-energy peak can reach 1.3 cm at the entrance of the first quadrupole, if $\Delta y = 6$ nm at the interaction point. Even in that case, the transport of the disrupted beam and the same-sign charged particles of the coherent pairs from the exit of the vertical chicane to the first refocusing quadrupole remains loss free.

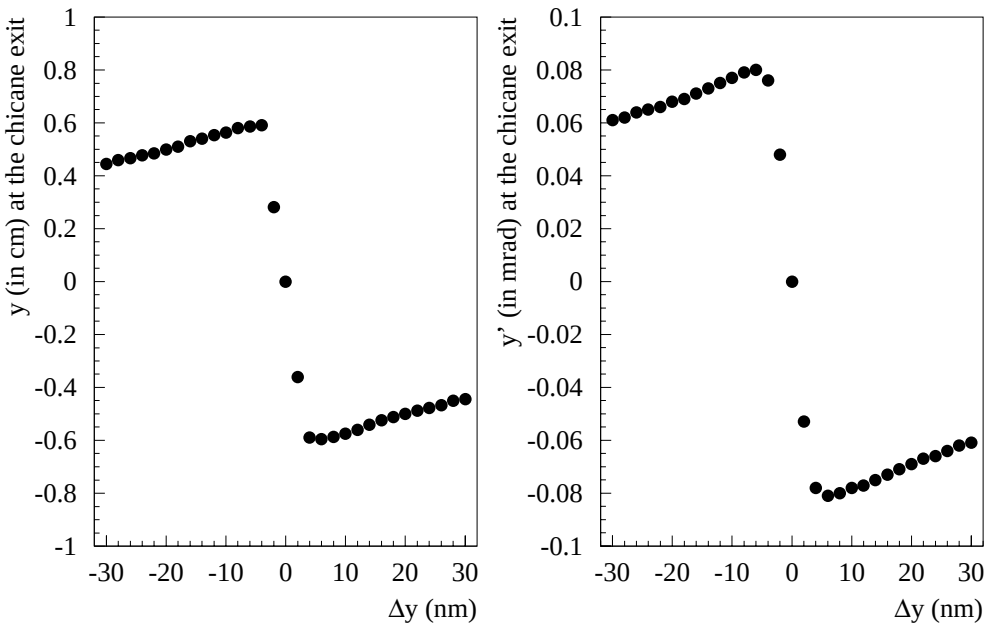

Figure 27: Vertical position and angle of the high-energy peak of the disrupted beam at the exit of the chicane, as a function of the vertical offset in position at the interaction point. The reference path (with $y = 0$ and $y' = 0$) corresponds to the disrupted beam obtained in the case of ideal e^+e^- collisions.

If the high-energy peak of the disrupted beam does not pass through the centre of the 16 quadrupoles, then it will receive a vertical kick that has a refocusing effect and therefore partly compensates the kick received during the bunch crossing. As a result, a small vertical offset at the interaction point does not lead to additional losses in or between the quadrupoles. Figure 28 shows how the vertical displacement of the high-energy peak at the exit of the last quadrupole, as well as its angle, vary with Δy.

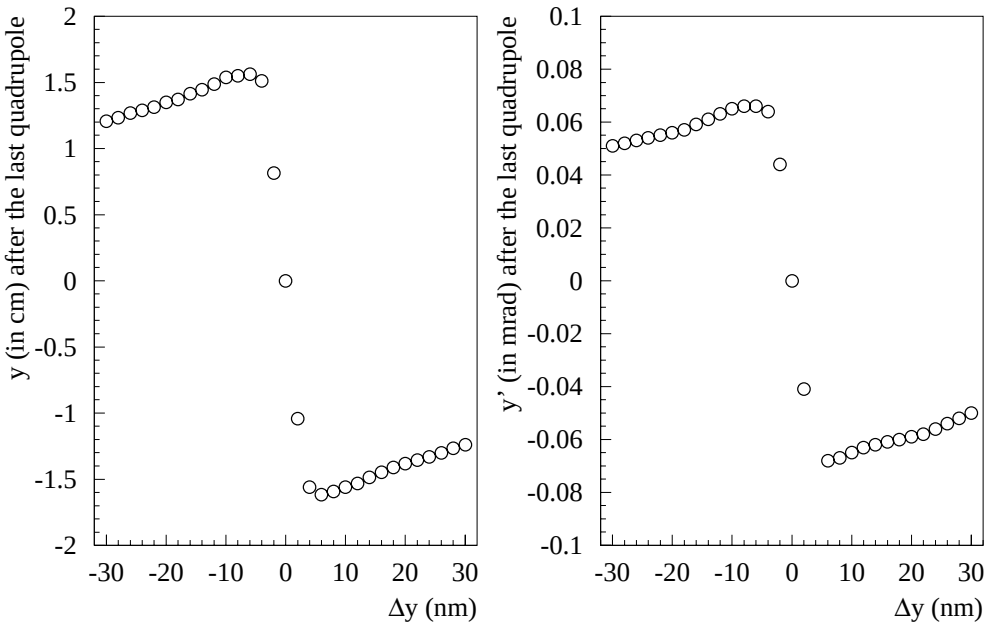

Figure 28: Same as in Figure 27, but these plots are obtained at the exit of the last refocusing quadrupole.

With $\Delta y = 6$ nm at the interaction point, the angle of the high-energy peak is 0.07 mrad after the last quadrupole (its sign depends on the post-collision line that one considers). This is 0.01 mrad smaller than the angle at the entrance of the refocusing region. The vertical displacement is 1.6 cm at the exit of the last quadrupole and becomes close to 2 cm at the dump window. Without the refocusing quadrupoles, these values would be 1.7 cm and 2.2 cm, respectively.

Having studied the transport of the high-energy peak of the disrupted beam, let us now focus on the low-energy tail. Figure 29 shows that, as a result of the vertical displacement of the disrupted beam, the low-energy edge becomes closer to the vacuum pipe wall in one of the post-collision lines. Nevertheless, its transverse apertures are still large enough to allow a loss free transport from the last quadrupole to the dump window. If the safety margins were to be improved, several technical solutions could be easily implemented in the design of the CLIC post-collision line. For instance, the vertical dimension of the dump window can be increased by a few cm. Alternatively, the dump can be moved further away from the interaction point, so that the low-energy edge of the disrupted beam, which has $y' > 0$, gets closer to the high-energy peak. Finally, one may install more refocusing quadrupoles along the post-collision line, in order to further compensate for the kick received during the bunch crossing (in that case, one may also need to slightly increase the horizontal dimension of the dump window).

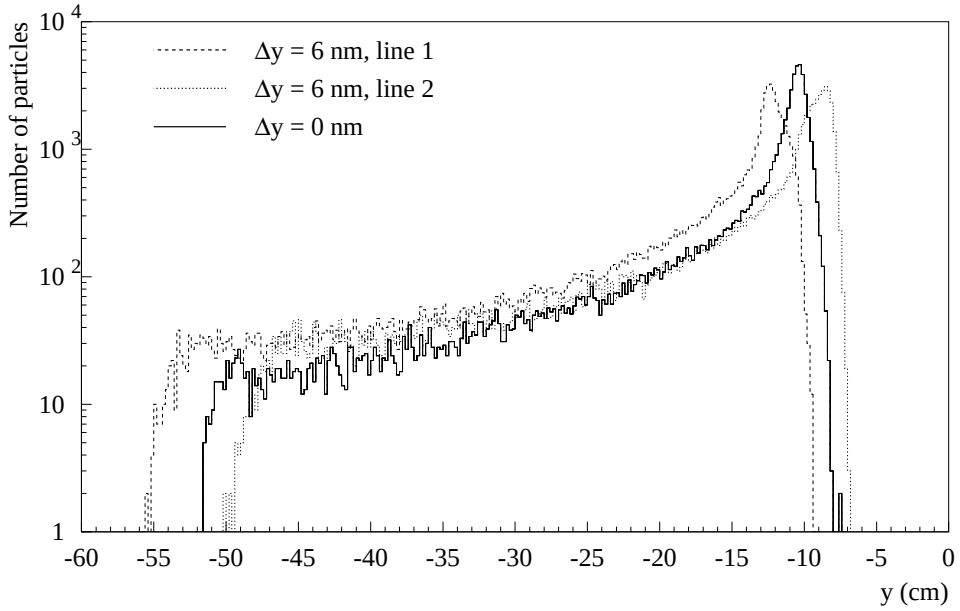

Figure 29: Vertical profile of the disrupted beam and the same-sign charged particles of the coherent pairs at the dump window, in the case of ideal e^+e^- collisions (full line) or with $\Delta y = 6$ nm (dashed and dotted lines).

Since the beamstrahlung photons do not carry any electric charge, they do not receive any kick during the bunch crossing. Hence, they always arrive at the same position on the dump window (or on screens placed along the post-collision lines). By measuring the number and/or density of photons, as well as their transverse spot size, it is possible to retrieve useful information about the small vertical position offset at the interaction point. For instance, the left-hand side plot of Figure 30 shows how the vertical rms size of the beamstrahlung photon cone at the dump window varies with the vertical position offset at the interaction point.

The right-hand side plot of Figure 30 shows the dependence on Δy for the power losses of the beamstrahlung photons along the last section of the CLIC post-collision line, i.e. downstream of the vertical chicane (note that only a fraction of the power is actually deposited in the vacuum pipe wall). By installing an additional collimator just after the vertical chicane, one can collect the photons that would not reach the dump window. For this purpose, its aperture should have an elliptical shape with a vertical semi-axis of 2.5 cm at most. Also, it should only stop particles in the upper part of the vacuum pipe and must not disturb the transport of the charged beams. The measurement of the power deposited in this additional collimator could then be used in order to derive the vertical position offset at the interaction point.

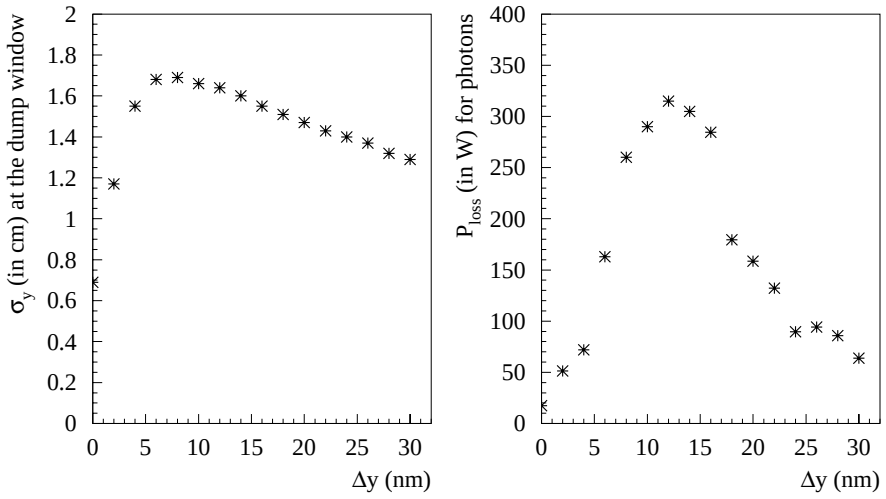

Figure 30: Vertical rms size of the beamstrahlung photon cone (left) and associated power losses downstream of the vertical chicane (right), as a function of the vertical offset in position at the interaction point.

5.2 Performance of the CLIC post-collision line with a vertical angular offset at the interaction point

Having studied the influence of a vertical position offset at the interaction point on the outgoing beam distributions and the power losses along the CLIC post-collision line, we now set Δy to zero and we introduce a small vertical angular offset $\Delta y'$. Its first impact on the outgoing beams is a non-zero mean value for the y' distributions of the secondary particles (beamstrahlung photons and coherent pairs) after the collision. Meanwhile, note that the main outgoing beam always has a symmetric y' profile, with a zero mean value. An enhancement of the disruption process also occurs, which translates into a larger number of low-energy particles, beamstrahlung photons and coherent pairs, as well as increased vertical rms beam sizes. The effects of the vertical angular and position offsets on the outgoing beams are not very different, therefore we expect similar impacts on the transport and the power losses. Note however that the symmetry between the two post-collision lines is conserved with an angular offset at the interaction point. On the other hand, we must consider both positive and negative values of $\Delta y'$, since they may affect the performance of the post-collision line in different ways.

Upstream of the separation region, the additional power losses due to an angular offset at the interaction point mostly occur in the collimators between the extraction magnets, and not in the dipoles themselves. For the disrupted beam, the power losses reach 150 W per collimator between the first and the second magnets. For the two collimators placed between the second and the third magnets, the losses can go up to 400 W. Finally, each

collimator located between the third and the fourth magnets receive up to 800 W. For each type of particles in the coherent pairs, these numbers become 100 W, 150 W and 300 W, respectively. Such values are usually obtained when $\Delta y' \geq 0.1$ mrad. With a non-zero $\Delta y'$ at the interaction point, the power losses are mostly due to the disruption enhancement, and thereby the amount of low-energy particles. Indeed, the effect of a non-zero mean value of the y' distributions is only relevant for the coherent pairs and the bending angle provided by the extraction magnets rapidly becomes much larger than the mean value of y' just after the bunch crossing.

Downstream of the separation region, we first focus on the particles of the coherent pairs with the wrong-sign charge. The left-hand side plot of Figure 31 shows how the beam power passing through the dump window varies with $\Delta y'$. The right-hand side plot indicates that the fraction of the beam power is always about 75%, as in the case of a non-zero vertical position offset at the interaction point. Our results also suggest that the sign of $\Delta y'$ does not have a significant impact, which is consistent with the fact that the transverse distributions of the coherent pairs downstream of the four extraction magnets are mostly determined by the energy spread and that the value of y' just after the bunch crossings does not have a sizeable effect.

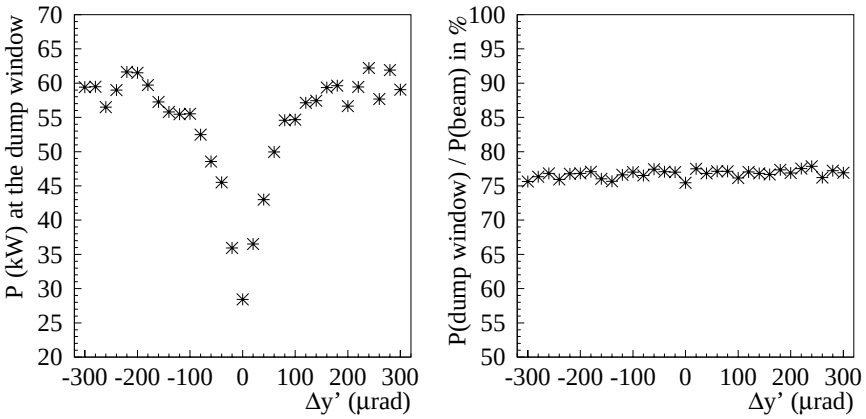

Figure 31: Beam power passing through the dump window of the extraction line of the wrong-sign charged particles of the coherent pairs, as a function of the vertical angular offset at the interaction point.

As for the disrupted beam and the component of the coherent pairs with the same charge, the losses downstream of the separation region only come from the absorption of low-energy particles by the five collimators, see Figure 32. Again, our results do not significantly depend on the sign of $\Delta y'$, since the vertical beam profiles are dominated by the contribution of the energy spread. As in the case of a small position offset at the interaction point, the transport through the C-type magnets remains loss free.

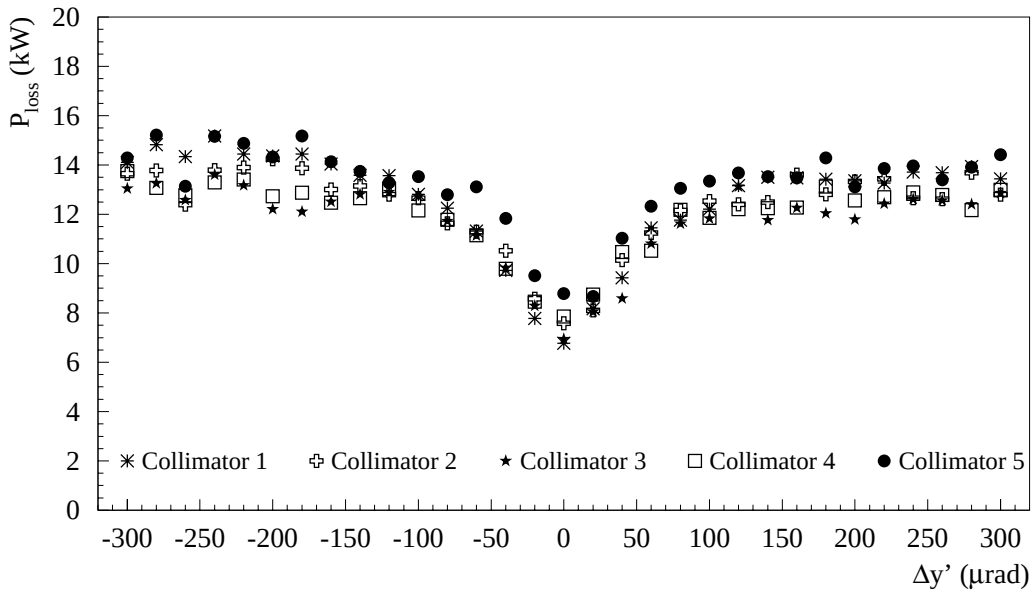

Figure 32: Power losses in the collimators placed at the beginning of the transport line for the disrupted beam and the same-sign charged particles of the coherent pairs, as a function of the vertical angular offset at the interaction point.

Just like after the bunch crossing, the y' distribution of the high-energy peak always has a zero mean value at the exit of the chicane, and therefore does not depend on the angular offset at the interaction point (this is true as long as $\Delta y = 0$ and that both incoming beams have the same deviation $\Delta y'/2$). In these conditions, only the shape of the vertical beam profile (and thus its rms value) may be used to measure the angular offset, and not its position along the post-collision line or at the dump window. This is illustrated by Figure 33. Note that the shape of the low-energy tails is slightly different with and without an angular offset at the interaction point, which is consistent with an enhancement of the disruption process and an increase of the number of coherent pairs when $\Delta y' \neq 0$.

Let us now focus on the beamstrahlung photons. They are emitted by the incoming electron and positron beams as soon as they start to experience some deflection during the bunch crossing. So, these photons still carry some information about the initial y' distribution of the colliding beams. As a result, both the position and the shape of the beamstrahlung photon cone at the dump window depend on the angular offset at the interaction point. This is illustrated by Figure 34. With $\Delta y' = \pm 0.1$ mrad, the vertical displacement of the beamstrahlung photon cone at the dump window is about 2 mm, and a significant distorsion is observed.

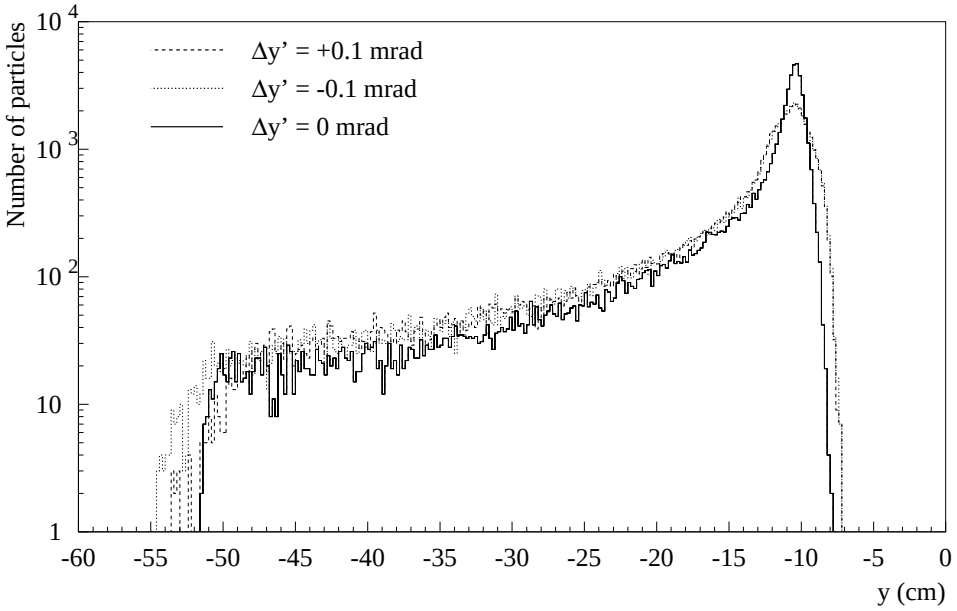

Figure 33: Vertical profile of the disrupted beam and the same-sign charged particles of the coherent pairs at the dump window, in the case of ideal e^+e^- collisions (full line) or with $\Delta y' = \pm 0.1$ mrad (dashed and dotted lines).

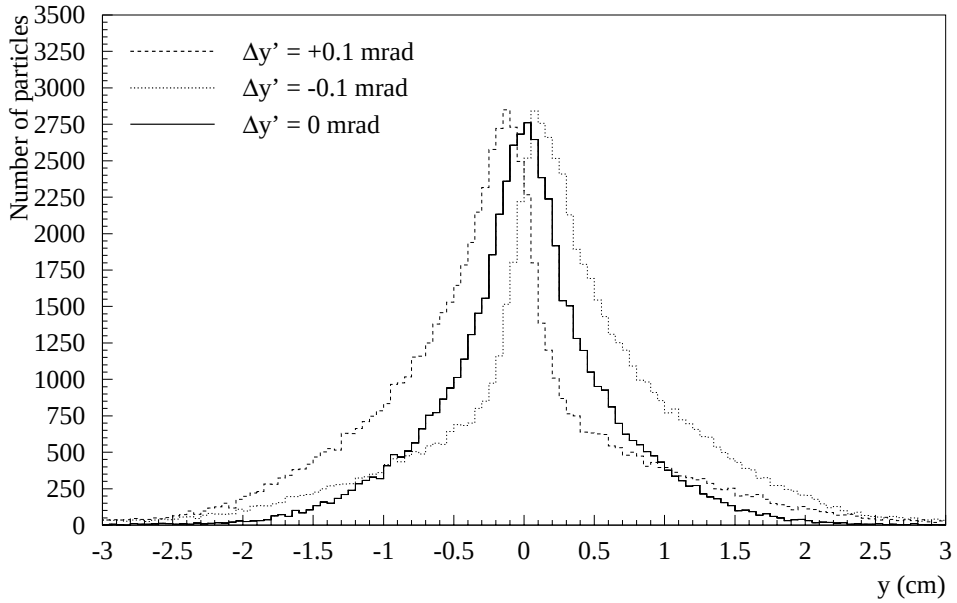

Figure 34: Vertical profile of the beamstrahlung photons at the dump window, in the case of ideal e^+e^- collisions (full line) or with $\Delta y' = \pm 0.1$ mrad (dashed and dotted lines).

Figure 35 shows the variation with $\Delta y'$ of the accumulated power losses due to the beamstrahlung photons between the exit of the chicane and the dump window. Note that the number of lost photons strongly depends on the sign of $\Delta y'$. Also, as already pointed out, the photons that do not reach the end of the post-collision line may be collected and measured in an additional collimator placed just after the chicane. This would indeed help derive the vertical angular offset at the interaction point.

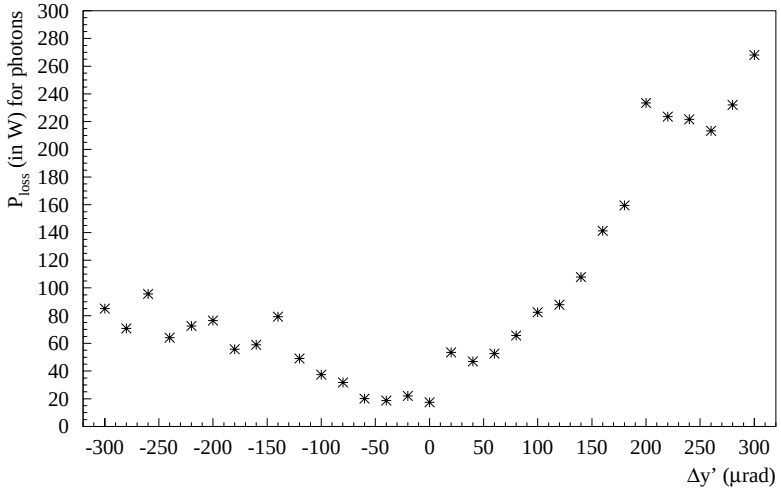

Figure 35: Power losses due to the beamstrahlung photons downstream of the vertical chicane, as a function of the vertical angular offset at the interaction point.

6 Conclusion and outlooks

This paper presents a conceptual design of the post-collision line for the nominal CLIC machine. It first separates the various components of the outgoing beam in four compact extraction magnets, which provide a total bending angle of 3.2 mrad at 1.5 TeV. The charged particles with $\delta < -0.95$ are absorbed in collimators placed between the dipoles, which ensures that the beam transport through the extraction magnets remains loss free. Following their physical separation from the other beam components, the particles of the coherent pairs with the wrong-sign charge are immediatly brought to their dump. The energy spectrum of the coherent pairs is derived from the vertical distribution of the wrong-sign charged beam, before it becomes too large to fit inside a vacuum pipe with reasonable dimensions. As for the disrupted beam and the beamstrahlung photons, they are transported inside the same vacuum pipe to a common dump, located about 250 m donwstream of the interaction point. The bend provided by the four extraction magnets is followed by a bend in the opposite direction, in order to eventually have $D'_y = 0$. For this purpose, we use four C-type dipole magnets. All beamstrahlung photons and all

charged particles with $\delta > -0.85$ pass through the vertical chicane and reach the dump. The lost particles are absorbed in five collimators placed between the separation region and the first C-type magnet. At the exit of the chicane, the low-energy particles of the disrupted beam, which still have $y' < 0$, receive a positive kick when passing through 16 vertically focusing quadrupoles (meanwhile, the high-energy core of the beam remains unaffected). This allows some flexibility in the design of the last section of the post-collision line, including the dump window, because the vertical rms size of the disrupted beam after the refocusing region decreases with the distance from the interaction point to the dump. An accurate analysis of the final transverse beam profiles allows to derive relevant information on the e^+e^- collisions. In particular, small vertical beam-to-beam offsets in position and/or angle, which affect the disruption process, can be identified by measuring the displacement and/or the distorsion of the outgoing beams. We have also shown that these offsets lead to additional losses along the post-collision line, however these will only occur in the collimators.

After having generated the CLIC outgoing beams with GUINEA-PIG, our design of the post-collision line is entirely based on DIMAD particle trackings. This program allows to follow a large number of electrons, positrons and beamstrahlung photons, without using large amounts of memory and/or computing time. However, it does not simulate the interactions of particles with the surrounding matter, once they have left the vacuum pipe or after hitting a collimator. Furthermore, DIMAD does not accurately simulate synchrotron radiation. For a complete estimation of the performance of the CLIC post-collision line, one will need to run BDSIM simulations [16]. This program is written in GEANT4 [17] and thereby provides a toolkit to fully simulate the interactions between the lost particles and the surrounding matter. This is crucial when estimating the background due to back-scattered particles at the interaction point. Other important issues are the constraints for the design of the dump window. These were only briefly discussed in this paper, and should be analysed more accurately in a dedicated study. Also, the design of the collimators should be performed, as they will have to absorb particles with an energy of up to a few hundred GeV. Finally, the integration of the post-collision line into the whole CLIC complex, and in particular encumbrance issues resulting from the proximity of the incoming beam line with its magnetic elements, must be carefully adressed in future studies.

Acknowledgements

This work is supported by the Commission of the European Communities under the 6^{th} Framework Programme "Structuring the European Research Area", contract number RIDS-011899.

The author wishes to thank D. Reistad and V. Ziemann (Uppsala University), as well as T. Zickler and J. Borburgh (CERN) for fruitful discussions, especially regarding magnet technology and design.

References

[1] I. Wilson, "The compact linear collider CLIC", CLIC note 617, CERN-AB-2004-100, published in Phys. Rep. 403-404 (2004) 365-378.

[2] D. Schulte and F. Zimmermann, "The crossing angle in CLIC", CLIC note 484, CERN-SL-2001-043 (AP), CERN-PS-2001-038 (AE), presented at PAC'01, Chicago, USA.

[3] R. Arnold, K. Moffeit, Y. Nosochkov, W. Oliver, A. Seryi, E. Torrence and M. Woods, "Design of ILC extraction line for 20 mrad crossing angle", presented at PAC'05, Knoxville, USA.

[4] A. Ferrari, "Power losses of a nominal CLIC beam in the ILC 20 mrad extraction line", EUROTeV-Report-2006-019, CLIC note 662.

[5] F. Tecker *et al.*, CLIC note 627.

[6] D. Schulte, TESLA-97-08 (1996).

[7] P. Chen, "Coherent Pair Creation from Beam-Beam Interaction", SLAC-PUB 5086 (1989).

[8] www-project.slac.stanford.edu/ilc/acceldev/beamparameters.html

[9] http://www.slac.stanford.edu/accel/ilc/codes/dimad

[10] K.L. Brown, D.C. Carey, Ch. Iselin and F. Rothacker, "TRANSPORT, a computer program for designing charged particle beam transport systems", SLAC 91, NAL 91 and CERN 80-04.

[11] G.E. Fisher, "Iron dominated magnets", SLAC-PUB-3726, 90-98.

[12] M. Seidel, "An Exit Window for the TESLA Test Facility", DESY-TESLA 95-18.

[13] T. Zickler, private communications.

[14] R. Veness, B. Goddard, L. Massida, S.J. Mathot and A. Presland, "Design of the LHC beam dump entrance window", LHC-PROJECT-Report-965, presented at EPAC'06 , Edinburgh, Scotland.

[15] V. Ziemann, *Ideas for an Interferometric Thermometer*, Nucl. Inst. and Meth. A564 (2006) 587-589.

[16] http://flc.pp.rhul.ac.uk/bdsim.html

[17] GEANT4 Collaboration (S. Agostinelli et al), "GEANT4: a simulation toolkit", Nucl. Instr. and Meth. NIM A 506 (2003), 250-303.